Deconvolution by Matching Pursuit using spline wavelet packets dictionaries

Amir Z. Averbuch Valery A. Zheludev and Marie Khazanovsky

School of Computer Science

Tel Aviv University

Tel Aviv 69978, Israel

September 17, 2010

Abstract

We present an efficient method that restores signals from strongly noised blurred discrete data. The method can be characterized as a regularized matching pursuit (MP), where dictionaries consist of spline wavelet packets and their sampled convolutions with the blurring kernel. It combines ideas from spline theory, wavelet analysis and greedy algorithms. A unified computational engine, which enables to construct a versatile libraries of spline wavelet packet dictionaries and efficient implementation of the algorithm, is the Spline Harmonic Analysis (SHA). SHA imposes harmonic analysis methodology onto spline spaces. It is especially applicable to convolution operations. The use of splines enables to map the discrete noised data into spaces of continuous functions, which approximate the sought after solution in the proper smoothed class. The main distinction from the conventional MP is that different dictionaries are used to test the data and to approximate the solution. In addition, the oblique projections of data onto dictionary elements are used instead of orthogonal projections, which are used in conventional MP. The slopes of the projections and the stopping rule for the algorithm are determined automatically. Experimental results exhibit a high efficient algorithm. The coherent structure of the signals, which were subjected to the strong blurring and immersed into deep noise, were extracted.

1 Introduction

Deconvolution extracts a signal from undesired convolution. Theoretically, it is the solution f of an integral equation

$$g(x) = \int_{-\infty}^{\infty} h(x-y)f(y)dy = \mathbf{H}f,$$

and of similar equations in several dimensions, where the data function g and the kernel h are known. For example, sources of an unwanted convolution effect can be the measurement of a signal by an instrument, transmission of the signal through a channel, image blurring, echoes in telephone calls, penetration of seismic signals through the earth thickness, to name a few. Thus, deconvolution algorithms are needed in many scientific and engineering disciplines including image processing, seismic processing, spectroscopy, geophysics, chromatography, communication theory, tomography, remote sensing, 3D deconvolution microscopy [8, 30, 31].

The convolved signal, which is measured in a discrete set of points and errors (noise), is inevitable. The straightforward inversion of the convolution operator $\mathbf{H}$ leads to a strong amplification of the error component. Therefore, deconvolution is an ill-posed problem. Due to the ill-posedness and the diversity of applications, no universal deconvolution algorithm exists. Starting from the classical work by Wiener [33], a number of approaches have been suggested to overcome the instability of the solutions [32]. Recently, wavelet based methods were used [14, 12, 15]. Many efficient deconvolution algorithms are based on the Tikhonov regularization method [27, 28] and related schemes [22, 17], where the solutions stabilization is achieved by quadratic constrains. For example, regularized locally adaptive kernel regression was presented in [26]. Non-quadratic constrains, which result in the solutions sparsity, are investigated in [10]. Wavelets and regularization methods, which are based on the Fourier transform, were combined in [11, 21, 29, 9].

The Fourier transform is widely used in convolution problems. The reason is that exponential functions, which form a basis for the transform, are the eigenfunctions of the convolution operator. However, in signal processing applications, some gap exists between continuous convolution that physical devices produce and the discreteness of the available data. Spline functions enable to bridge this gap by mapping the discrete data into spaces of smooth functions ([3]). An additional advantage for using splines for deconvolution application lies in their abilities to effectively control the smoothness of the solution.

We propose a spline-based scheme for solving the convolution equation. The scheme modifies the matching pursuit (MP) algorithm [19, 13, 23]. The MP is a greedy algorithm, which performs successive approximation of a signal by iteratively testing the available data by elements from a redundant dictionary of waveforms. Our dictionaries consist of spline wavelet packets. Due to the great variability of shapes and frequency contents of these wavelet packets, they may serve as

universal building blocks to approximate various functions. In addition, they are well compatible with the convolution operator.

The computational engine, which enables us to design the dictionaries and to efficiently implement the algorithms, is the so-called Spline Harmonic Analysis (SHA). Originally, this technique was presented in its final form in [39] but some of its components were exposed in [35, 24, 36]. It relies on orthogonal bases in spline spaces whose properties are similar to Fourier harmonics properties. In particular, the splines, which form the bases, are, in some generalized sense, the eigenfunctions of the convolution operator. Thus, these bases yield an appropriate environment for solving convolution-related problems with discrete input data ([3, 38]). The usage of these bases provides explicit solutions and tools to flexibly control their properties. In addition, this harmonic analysis may serve as a framework for the construction of wavelet transforms in spline spaces [39, 41, 2]. Using the technique described in [39], we constructed the dictionaries consisting of spline wavelet packets of arbitrary orders, which our MP algorithm is based on.

In this paper, we present the Regularized MP (RMP) algorithm that combines MP, which uses the spline wavelet packets dictionaries, with a regularization methodology.

The innovations in our method are:

Dictionaries: RMP uses a pair of dictionaries: one, continuous, is used to approximate the solution. It consists of translations of spline wavelet packets. The other, discrete, is used for testing the data. It consists of wavelet packets that are convolved with a kernel, which are sampled on a grid.

Computational engine: Spline Harmonic Analysis (SHA) whose basic operation is the fast Fourier transform (FFT). It is important that the application of the FFT to the data is implemented only at the first iteration. At subsequent iterations, the correlation coefficients are updated without resorting to FFT. When the iterations are stopped, the inverse FFT is applied to obtain an explicit time domain representation of the solution. Such a scheme allows to operate on large data arrays that are common in multidimensional cases.

Regularization: The orthogonal projection of the data vectors onto the testing dictionary elements, as it is common in MP, may result in solution instability. To avoid this, we use oblique projections, where the slopes for each dictionary element are determined automatically from the data during the iterative process.

Stopping rule: Relative contributions of the coherent signal and the noise into the input data are automatically evaluated during the iterative process. When the noise contribution in the iterative process becomes overwhelming, the algorithm is halted.

This approach proved to be efficient for strongly noised blurred 1D signals. A slight modification turns the proposed deconvolution algorithm into a powerful denoising algorithm.

The paper is organized as follows. Section 2 provides a preliminary information on the conventional MP and short outline of SHA. In Section 3, spline wavelet packets are constructed. Section 4 describes the RMP algorithm. A few experimental results are presented in Section 5. The paper is concluded by a brief discussion and a glossary of used notations.

2 Preliminaries

If the involved functions are compactly supported then the deconvolution problem can be reduced to finding an N-periodic solution of the equation

$$g(x) = h(x) \star f(x) = \int_0^N h(x-y)f(y)dy, \tag{2.1}$$

where the the unknown function $f(x)$, the blurring kernel $h(x)$ and the data function $g(x)$ are N-periodic. We assume that the kernel h and the data function g have continuous derivatives. We assume that the data is sampled on the grid $\{k\}$. The samples are corrupted by a random noise $\mathbf{e} = \{e_k\}$. In addition, we assume that only samples from the periodic kernel h on the grid $\{k\}$ are known. Thus, we have at our disposal N-periodic arrays $\mathbf{z}$ and $\mathbf{h}$ such that $\mathbf{z} = \{z_k\} = \{g(k)+e_k\}$, $\mathbf{h} \stackrel{\Delta}{=} \{h(k)\}$, $k = 0, ..., N-1$.

In the sequel, $\omega \stackrel{\Delta}{=} e^{2\pi i/N}$. The Discrete Fourier Transform (DFT) of a vector $\mathbf{a} \stackrel{\Delta}{=} \{a_k\}_{k=0}^{N-1}$ and its inverse (IDFT) are $\hat{a}(n) \stackrel{\Delta}{=} \sum_{k=0}^{N-1} \omega^{-nk} a_k$, and $a_k = N^{-1} \sum_{n=0}^{N-1} \omega^{nk} \hat{a}(n)$, respectively. The circular discrete convolution $\mathbf{c} \stackrel{\Delta}{=} \{c_k\}_{k=0}^{N-1}$ of N-periodic signals $\mathbf{a} \stackrel{\Delta}{=} \{a_k\}$ and $\mathbf{b} \stackrel{\Delta}{=} \{b_k\}$ is $\mathbf{c} = \mathbf{a} * \ \mathbf{b} \Longleftrightarrow c_k = \sum_{l=0}^{N-1} a_{k-l} b_l,$. Then, the DFT of the convolution is $\hat{c}(n) = \hat{a}(n)\hat{b}(n)$.

We propose to find approximated solutions to Eq. (2.1) as linear combinations of periodic spline wavelet packets. For this, we utilized the Spline Harmonic Analysis (SHA), which provides a unified computational scheme for explicit construction of wavelet packets and a efficient implementation of the algorithm.

2.1 Outline of the Matching Pursuit (MP) scheme

2.1.1 Conventional MP

The MP algorithm [19] approximates a function in a redundant dictionary of functions (features) by using a greedy strategy. The features, which best match the signal, are selected one by one from the dictionary that subsequently improves the approximation.

Let $\mathbf{D} = \{\theta_\gamma\}_{\gamma=1}^{P}$ be a dictionary with P elements and g be a given signal. We begin with the approximation $g^0 \triangleq 0$ and the remainder $z^0 \triangleq g$. In the first step of MP, the orthogonal projections $z_\gamma^0 = \alpha_\gamma \, \theta_\gamma / \|\theta_\gamma\|$ of the remainder z^0 onto the normalized dictionary elements are calculated where $\alpha_\gamma = \langle z_0, \theta_\gamma \rangle / \|\theta_\gamma\|$. Assume that the projection onto the element $\theta_{\underline{\gamma}}$ is the strongest (that is $\underline{\gamma} = \arg\max_\gamma |\alpha_\gamma|$). Denote $\alpha^1 \triangleq \alpha_{\underline{\gamma}}$, $\theta^1 \triangleq \theta_{\underline{\gamma}}$. Define the first approximation as $g_1 = g_0 + \mu^1 \, \theta^1$ and the residual as $z_1 = z_0 - \mu^1 \, \theta^1$, where $\mu^1 \triangleq \alpha^1 / \|\theta^1\|$. Then, we iterate the procedure by using z_1 instead of z_0. It results in α^2, θ^2 and $\mu^2 \triangleq \alpha^2 / \|\theta^2\|$. The second approximation is $g_2 = g_1 + \mu^2 \, \theta^2$ and the residual is $z_2 = z_1 - \mu^2 \, \theta^2$. After S iterations, we have $g = g_S + z_S = \sum_{s=0}^{S-1} \mu^s \, \theta^s + z_S$.

Loosely speaking, the idea behind the MP is: The successive residuals z_s are tested for the presence of a coherent structure by elements from the dictionary $\mathbf{D}$. If a coherent component, which is close to some dictionary element present in the residual, then the projection of the residual onto this element is significant. Thus, this piece of the coherent structure is transferred from the residual to the approximation of the function g. If the noised version of the data is available then the residuals converge to the noise component of the data [13], which is non-coherent with all the dictionary elements. Otherwise they converge to zero [19].

2.1.2 MP for deconvolution

In our case, the function should be restored from its sampled convolution corrupted by noise (vector $\mathbf{z}$). This prevents the utilization of the standard MP scheme. However, we construct a pair of dictionaries and propose a modification of the MP algorithm, which enables to accurately approximate the original function $f(x)$ even when convolution blurring and noise are strong. The algorithm is implemented via the following steps:

- Approximation of the convolution kernel $h(x)$ by a spline $\chi(x)$.
- Construction of two dictionaries:

  Approximation dictionary $\mathbf{D}_A = \left\{\psi_k^{r,l}(x)\right\}$ consisting of one-sample shifts of spline wavelet packets from different resolution scales.

  Testing dictionary $\mathbf{D}_T = \left\{\Theta_k^{r,l}\right\}$, where the discrete signal $\Theta_k^{r,l}(i) = \theta_k^{r,l}(i)$ and $\theta_k^{r,l}(x) = \chi \star \psi_k^{r,l}(x)$ is the convolution of the wavelet packet $\psi_k^{r,l}(x)$ with the spline $\chi(x)$.
- Typically, the convolution kernel $h(x)$ is efficiently bandlimited. Therefore, spectra of some wavelet packets $\psi_k^{r,l}(x)$ actually do not overlap with the kernel spectrum. In order to avoid instability of the algorithm, we discard such wavelet packets and corresponding $\Theta^{\tilde{r},\tilde{l}}$ from the dictionaries.

- Evaluate the error vector $\mathbf{e}$ that is construct a vector $\tilde{\mathbf{e}}$, whose characteristics are similar to the characteristics of $\mathbf{e}$.
- Put $f^0(x) \equiv 0$, $\mathbf{z}^0 = \mathbf{z}$.
- Find *oblique* projections of $\mathbf{z^0}$ onto the normalized $\Theta_k^{r,l}$:

$$\mathbf{z}_k^{0,r,l}(\rho) = \alpha_k^{r,l}(\rho)\frac{\Theta_k^{r,l}}{\|\theta^{r,l}\|}, \quad \alpha_k^{r,l}(\rho) = \frac{\left\langle \Theta_k^{r,l}, \mathbf{z}^0 \right\rangle}{\|\theta^{r,l}\|}\left(1 - \frac{\left|\left\langle \theta^{r,l}, \tilde{\mathbf{e}} \right\rangle\right|}{\left|\left\langle \Theta_k^{r,l}, \mathbf{z}^0 \right\rangle\right|}\right).$$

- Let $\underline{r}, \underline{l}, \underline{k} = \arg\max_{r,l,k} \left|\alpha_k^{r,l}(\rho)\right|$.
- Denote $\mu^1 \triangleq \alpha_{\underline{k}}^{\underline{r},\underline{l}}/\|\theta^{r,l}\|$, $\psi^1(x) \triangleq \psi_{\underline{k}}^{\underline{r},\underline{l}}(x)$ and $\Theta^1 \triangleq \Theta_{\underline{k}}^{\underline{r},\underline{l}}$. Then, we put $\mathbf{z}^1 = \mathbf{z}^0 - \mu^1\Theta_{\underline{k}}^{\underline{r},\underline{l}}$, $f^1(x) = f^0(x) + \mu^1\psi_{\underline{k}}^{\underline{r},\underline{l}}(x)$.
- Then, the procedure is iterated using $\mathbf{z}^1$ instead of $\mathbf{z}^0$ and so on.
- The subsequent iterations of the algorithm extract pieces of coherent structure from the data signal $\mathbf{z}$. Thus, the noise-to-signal ratio tends to one and the oblique projection coefficients tend to zero. When they become less than a predefined threshold, the iterations are aborted.
- As a result, the function $f(x)$ is approximated by a finite linear combination of spline wavelet packets.

A unified scheme for construction of dictionaries, implementation of the algorithm and explicit expression of the solutions is provided by the so-called Spline Harmonic Analysis (SHA).

2.2 Outline of SHA

2.2.1 Periodic splines

The centered B-splines of the first order on the grid $\{k\}$ is

$$\widetilde{B}^1(x) \triangleq \begin{cases} 1, & x \in [-1/2, 1/2], \\ 0, & \text{otherwize.} \end{cases}$$

The periodization of the spline $B^1(x) \triangleq \sum_{l\in\mathbb{Z}} \widetilde{B^1}(x + lN)$ is called the N-periodic B-spline of the first order on the grid $\{k\}$. The Fourier expansion of the B-spline is:

$$B^1(x) = \frac{1}{N}\sum_{n=-\infty}^{\infty} C_n(B^1)\, e^{2\pi i n x/N}, \quad C_n(B^1) \triangleq \int_0^N e^{-2\pi i n x/N}\, B^1(x)dx = \frac{\sin(\pi n/N)}{\pi n/N}.$$

The periodic B-spline of order p is defined via the iterated circular convolution $B^p(x) \triangleq B^1(x) \star B^{p-1}(x)$. Respectively, its Fourier coefficients are

$$C_n(B^p) = \left(C_n(B^1)\right)^p \Longleftrightarrow B^p(x) = \frac{1}{N} \sum_{n=-\infty}^{\infty} \left(\frac{\sin(\pi n/N)}{\pi n/N}\right)^p e^{2\pi i n x/N}.$$

The B-spline $B^p(x)$ is symmetric about zero and non-negative. Its support (up to periodization) is $(-p/2, p/2)$. The spline $B^p(x)$ consists of pieces of polynomials of degree $p-1$ that are linked to each other at the nodes $\{(k+p/2)\}$ such that $B^p(x)$ belongs to the space C^{p-2}.

Throughout the paper, we assume that the splines are of even order. Thus, the nodes coincide with the grid points. The definition of $B^p(x)$ implies that

$$B^p \star B^m(x) = B^{p+m}(x) \in C^{p+m-2}. \tag{2.2}$$

Translations of B-spline $B^p(x)$ form a basis in the space of N-periodic splines of order p, which have nodes on the grid $\{k\}$. We denote this space by ${}^p\mathcal{S}$. A spline $S^p(x) \in {}^p\mathcal{S}$ and its Fourier coefficients are

$$S^p(x) = \sum_{k=0}^{N-1} q_k \, B^p\left(x-k\right), \quad C_n(S^p) = \hat{q}(n)\, C_n(B^p) = \hat{q}(n) \left(\frac{\sin(\pi n/N)}{\pi n/N}\right)^p, \tag{2.3}$$

$$\hat{q}(n) \triangleq \sum_{k=0}^{N-1} \omega^{-kn} q_k, \quad q_k = \frac{1}{N} \sum_{n=0}^{N-1} \omega^{kn}\, \widehat{q}(n), \quad k, n = 0, 1, ..., N-1. \tag{2.4}$$

It follows from (2.2) that the convolution of two periodic splines

$$S_1^p \star S_2^m(x) = S_3^{p+m}(x) \in {}^{p+m}\mathcal{S} \subset C^{p+m-2}. \tag{2.5}$$

is a spline, whose order is equal to the sum of the orders of the convolved splines.

2.2.2 Exponential splines

There exist orthogonal bases in the spaces ${}^p\mathcal{S}$ of periodic splines, which resemble the Fourier basis of the space of periodic functions consisting of complex exponential functions. From now on, when there is no confusion, the indicator of order p will be omitted. Therefore, the notation $S(x) \in {}^p\mathcal{S}$ means that it is the N-periodic spline of order p on the grid $\{k\}$.

Assume that a spline $S(x) \in {}^p\mathcal{S}$ is represented as in Eq. (2.3). After substituting (2.4) into (2.3), we get

$$S(x) = \sum_{k=0}^{N-1} B(x-k) \frac{1}{N} \sum_{n=0}^{N-1} \omega^{nk} \hat{q}(n) = \frac{1}{N} \sum_{n=0}^{N-1} \xi_n \, \beta_n(x), \tag{2.6}$$

where the *exponential splines* $\beta_n^p(x)$ are defined as

$$\beta_n^p(x) \triangleq \sum_{k=0}^{N} \omega^{nk} \, B^p(x-k) = \sum_{k=0}^{N-1} \omega^{-nk} \, B^p(x+k) \tag{2.7}$$

and the coordinates $\xi_n = \widehat{q}(n)$.

The functions $\beta_n(x)$ are the N-periodic splines from the space ${}^p\mathcal{S}^p\mathcal{S}$, whose coefficients in the B-spline basis are $\{\omega^{nk}\}$. The spline sequence $\{\beta_n(x)\}$ is N-periodic with respect to n. Thus, the spline $\beta_n(x)$ can be interpreted as a periodic version of the Zak Transform ([16, 34]) of the B-spline $B(x)$. The non-periodic exponential splines were introduced by Schoenberg [25], p.17.
The Fourier coefficients of exponential splines are calculated using Eqs. (2.3) and (2.7):

$$C_m(\beta_n^p) = C_m(B^p) \sum_{k=0}^{N-1} \omega^{k(m-n)} = N\delta_m^n(\text{mod } N)\Big(\frac{\sin(\pi m/N)}{\pi m/N}\Big)^p, \tag{2.8}$$

where δ_m^n is the Kronecker delta. Then, the Fourier series expansion of $\beta_n^p(x)$ is:

$$\begin{aligned}\beta_n^p(x) &= \frac{1}{N}\sum_{m=-\infty}^{\infty} e^{2\pi imx/N} C_m(\beta_n^p) = \sum_{m=-\infty}^{\infty} e^{2\pi i(n/N+m)x}\left(\frac{\sin\pi(n/N+m)}{\pi(n/N+m)}\right)^p \\ &= (\sin(\pi n/N))^p \sum_{m=-\infty}^{\infty} \omega^{(n+mN)x}\left(\frac{1}{\pi(n/N+m)}\right)^p. \end{aligned} \tag{2.9}$$

For further use, we single out the sequence

$$\begin{aligned} u_n^p \triangleq \beta_n^p(0) &= \sum_{k=0}^{N-1} \omega^{-nk}\, B^p(k) = \sin^p(\pi n/N) \sum_{m=-\infty}^{\infty}\left(\frac{1}{\pi(n/N+m)}\right)^p \\ &= \frac{\sin^p(\pi n/N)}{(\pi(n/N))^p} + O(n^{-p}), \end{aligned} \tag{2.10}$$

which can be explicitly calculated by applying the DFT to the B-splines samples.

The sequences u_n^p are N-periodic and strictly positive. They are symmetric about $N/2$ where they attain their minimum. Their maxima, which are equal to 1, are attained at $\{kN\}_{k=-\infty}^{\infty}$. We display in Fig. 1 the sequence $\{u_n^p\}$ of order 4,8 and 12:

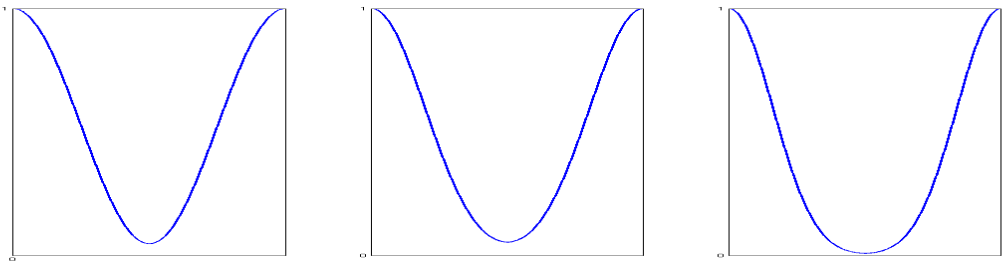

Figure 1: Sequences $\{u_n^p\}$ of order 4 (left), 8 (center) and 12 (right).

2.2.3 Properties of exponential splines

We list some properties of exponential splines, which are needed for the construction of the MP dictionaries and for the algorithm implementation.

Orthogonality: *The exponential splines* $\{\beta_n^p\}_{n=0}^{N-1}$ *form an orthogonal basis for the space* ${}^p\mathcal{S}$.

Proof: Equation (2.6) implies that the set $\{\beta_n^p\}_{n=0}^{N-1}$ form a basis for the space ${}^p\mathcal{S}$. It follows from Eq.(2.8) and from the Parseval's identity that the inner product of $\beta_n^p \in {}^p\mathcal{S}$ and $\beta_l^q \in {}^q\mathcal{S}$

$$\langle \beta_n^p, \beta_l^q \rangle = \int_0^N \beta_n^p x)\ \overline{\beta_l^q}(x)dx = \frac{1}{N} \sum_{m=-\infty}^{\infty} C_m(\beta_n^p)\ \overline{C_m(\beta_n^q)}$$

$$= \delta_l^n\ N\,(\sin(\pi n/N))^{p+q} \sum_{m=-\infty}^{\infty} \left(\frac{1}{\pi(n/N+m)}\right)^{p+q} = \delta_l^n\ N\ u_n^{p+q}, \tag{2.11}$$

$$\langle \beta_n^p, \beta_l^p \rangle = \delta_l^n\ N\ u_n^{2p}, \quad \|\beta_n^p\|^2 = N\ u_n^{2p}. \tag{2.12}$$

■

Shift: *The exponential splines are the eigenvectors of the shift operator.*

Proof: For all $d \in \mathbb{Z}$

$$\beta_n(x+d) = \sum_k^{j-r} \omega^{-nk}\, B^r(x+(d+k)) = \omega^{nd}\ \beta_n(x). \tag{2.13}$$

Convolution: *The convolution of two exponential splines is an exponential spline:*

$$\beta_n^p \star \beta_l^q = N\delta_n^l\ \beta_n^{p+q}. \tag{2.14}$$

Proof: If $f(x)$ and $h(x)$ are N-periodic functions and $g(x) = f(x) \star h(x)$ then $C(g)(r) = C(f)(r) \cdot C(h)(r)$. This property together with Eq. (2.8) imply Eq. (2.14). ■

Interpolation: *Exponential splines interpolate exponential functions at grid points.*

Proof: From Eq. (2.13) we get $\beta_n^p(k) = \omega^{nk}\ \beta_n^p(0) \Longrightarrow\ \beta_n^p(k)/u_n^p = e^{2\pi i n k/N}$. This property highlights the relationship between exponential functions and exponential splines.

Orthonormal bases: By normalizing the exponential splines $\{\beta_n^p\}$, we obtain the orthonormal basis $\{\gamma_n^p\}$ of ${}^p\mathcal{S}$. Equation (2.12) imply

$$\gamma_n^p(x) \stackrel{\Delta}{=} \sqrt{\frac{1}{N\ u_n^{2p}}}\ \beta_n^p(x). \tag{2.15}$$

The following relations exist

$$\gamma_n(x+d) = \omega^{nd}\ \gamma_n(x), \tag{2.16}$$

$$\gamma_n^p \star \gamma_l^q = \sqrt{N}\, U_n^{p,q}\, \delta_n^l\ \gamma_n^{p+q}, \quad U_n^{p,q} \triangleq \sqrt{\frac{u_n^{2(p+q)}}{u_n^{2p}\ u_n^{2q}}} \tag{2.17}$$

$$\frac{\sqrt{N\, u_n^{2p}}}{u_n^p}\ \gamma_n^p(k) = e^{2\pi i n k/N} \Longleftrightarrow \gamma_n^p(k) = \frac{w^{nk}}{\sqrt{N}}\, V_n^p, \quad V_n^p \triangleq \frac{u_n^p}{\sqrt{u_n^{2p}}}. \tag{2.18}$$

2.2.4 Representation of periodic splines by exponential spline basis

Equations (2.6) and (2.15) imply that the expansion of any spline $S^p \in {}^p\mathcal{S}$ via the orthonormal exponential spline basis is

$$S^p(x) = \sum_{k=0}^{N-1} q_k B^p(x-k) = \sqrt{\frac{1}{N}} \sum_{n=0}^{N-1} \sigma_n\, \gamma_n^p(x), \quad \sigma_n = \sqrt{u_n^{2p}}\, \hat{q}(n). \tag{2.19}$$

This expansion imposes a specific form of harmonic analysis methodology onto the spline space, where the exponential splines $\{\gamma_n^p(x)\}_{n=0}^{N-1}$ act as harmonics and the coordinates $\{\sigma_n\}\,,\ n = 0, ..., N-1$, which we refer to as to the SHA-spectrum of the spline $S^p(x)$, act as the Fourier coefficients. Many operations on splines are significantly simplified. We describe some of these operations.

Parseval identity: From Eq.(2.15) we get:

$$\|S^p\|^2 = \frac{1}{N} \sum_{n=0}^{N-1} |\sigma_n|^2. \tag{2.20}$$

Convolution: Let $S^p \in {}^p\mathcal{S}$ be represented as in Eq.(2.19) and $S^q(x) = N^{-1/2} \sum_{l=0}^{N-1} \eta_l\, \gamma_l^q(x) \in {}^q\mathcal{S}$. From Eq.(2.17), we have

$$S^p \star S^q(x) = \sum_{n,l=0}^{N-1} \sigma_n \eta_l\ \gamma_n^p \star \gamma_l^q(x) = \sqrt{\frac{1}{N}} \sum_{n=0}^{N-1} U_n^{p,q} \sigma_n\, \eta_n\ \gamma_n^{p+q}(x) \in {}^{p+q}\mathcal{S}. \tag{2.21}$$

Interpolation: Assume the spline $S^p(x)$ interpolates the data $\{z_k\}$ on the grid $\{k\}$. Then, by using Eq.(2.18), we get:

$$S^p(k) = \sqrt{\frac{1}{N}} \sum_{n=0}^{N-1} \sigma_n\ \gamma_n^p(k) = \frac{1}{N} \sum_{n=0}^{N-1} \sigma_n\, V_n^p\, \omega^{kn} = z_k \Longleftrightarrow \sigma_n = \frac{\hat{z}(n)}{V_n^p}. \tag{2.22}$$

Hence, the discrete Parseval identity follows:

$$\sum_{k=0}^{N-1} |S^p(k)|^2 = \frac{1}{N} \sum_{n=0}^{N-1} |\sigma_n\, V_n^p|^2 = \frac{1}{N} \sum_{n=0}^{N-1} |\sigma_n|^2 \frac{(u_n^p)^2}{u_n^{2p}}. \tag{2.23}$$

Remark 2.1. *If a spline $S^p(x) \in {}^p\mathcal{S}$ is represented as $S(x) = N^{-1/2} \sum_{n=0}^{N-1} \sigma_n \gamma_n^p(x)$, then its values at the grid points $\{k\}$, which are given in Eq. (2.22), are calculated by the inverse DFT. The values at the dyadic $\{2^{-r}k\}$ or the triadic $\{3^{-r}k\}$ rational points are calculated using fast subdivision algorithms [42, 43].*

Sampled convolution: By combining Eqs. (2.21) and (2.22), we get the grid samples of the convolution of two splines.

$$S^p \star S^q(k) = \frac{1}{N} \sum_{n=0}^{N-1} \omega^{kn}\, Q_n^{p,q} \sigma_n\, \eta_n, \quad Q_n^{p,q} \triangleq U_n^{p,q}\, V_n^{p+q} = \frac{u_n^{p+q}}{\sqrt{u_n^{2p}\, u_n^{2q}}}. \tag{2.24}$$

3 Construction of spline wavelet packets

We construct wavelet packets using the SHA technique, which was presented in section 2. The wavelet packets to be constructed are symmetric and well localized in both time and frequency domains. Orthogonality relations between groups of wavelet packets exist. In addition, the SHA technique simplifies the operations on these objects, especially operations related to convolution. The construction is based on the relations between the basis splines from the spline spaces of different resolution scales.

3.1 Split of the spline space

3.1.1 Spline spaces of different resolution scales

Denote by ${}^p\mathcal{S}^{r,0},\ r \in \mathbb{N}$, the space of N-periodic splines of even order p on the grid $\{2^r k\}$. This is $N/2^r$-dimensional space, where a basis consists of shifts of the grid $\{2^r k\}$ B-splines

$$B_r(x) \triangleq \frac{1}{N} \sum_{n=-\infty}^{\infty} \left(\frac{\sin(2^r \pi n/N)}{2^r \pi n/N} \right)^p e^{2\pi \mathrm{i} n x/N}. \tag{3.1}$$

A spline $S(x) \in {}^p\mathcal{S}^{r,0}$ can be represented as

$$S(x) = \sum_{k=0}^{N/2^r-1} q_k\, B_r\left(x - 2^r k\right), \quad C_n({}^pS^r) = \hat{q}(n)\, C_n(B_r) = \hat{q}(n) \left(\frac{\sin(2^r \pi n/N)}{2^r \pi n/N} \right)^p$$

$$\hat{q}(n) \triangleq \sum_{k=0}^{N/2^r-1} \omega^{-2^r kn} q_k, \quad q_k = \frac{2^r}{N} \sum_{n=0}^{N/2^r-1} \omega^{2^r kn}\, \widehat{q}(n), \quad k, n = 0, 1, ..., N/2^{N/2^r-1} - 1.$$

Obviously, ${}^p\mathcal{S}^{r,0} \subset {}^p\mathcal{S}^{r-1,0} \subset \ldots \subset {}^p\mathcal{S}^{0,0} \equiv {}^p\mathcal{S}$. Similarly to the space ${}^p\mathcal{S}$, we introduce the

orthogonal bases of exponential splines in the spaces ${}^p\mathcal{S}^{r,0}$:

$$ {}^p\beta_n^{r,0}(x) \triangleq \sum_{k=0}^{N/2^r-1} \omega^{2^r nk} B_r(x-2^r k) = 2^{-r} \sum_{m=-\infty}^{\infty} e^{2\pi \mathrm{i}(n/N+2^{-r}m)x} \left(\frac{\sin \pi(2^r n/N+m)}{\pi(2^r n/N+m)} \right)^p, \quad (3.2) $$

$$ {}^p u_n^r \triangleq {}^p\beta_n^{r,0}(0) = 2^{-r} \sum_{m=-\infty}^{\infty} \left(\frac{\sin \pi(2^r n/N+m)}{\pi(2^r n/N+m)} \right)^p. \quad (3.3) $$

A spline $S(x) \in {}^p\mathcal{S}^{r,0}$ is represented as

$$ S(x) = \frac{2^r}{N} \sum_{n=0}^{N/2^r-1} \xi_n \, {}^p\beta_n^{r,0}(x), \quad (3.4) $$

and the coordinates $\xi_n = \widehat{q}(n)$.

$$ \langle {}^p\beta_n^{r,0}, {}^q\beta_l^{r,0} \rangle = \delta_l^n \, 2^{-r} \, N^{\,p+q} u_n^r \Longrightarrow \|{}^p\beta_n^{r,0}\|^2 = 2^{-r} N^{\,2p} u_n^r. \quad (3.5) $$

Thus, the orthonormal basis splines in the space ${}^p\mathcal{S}^{r,0}$ are

$$ {}^p\gamma_n^{r,0}(x) \triangleq \sqrt{\frac{2^r}{N^{\,2p} u_n^r}} \, {}^p\beta_n^{r,0}(x), \quad S(x) = \sqrt{\frac{2^r}{N}} \sum_{n=0}^{N/2^r-1} \sigma_n^{r,0} \, \gamma_n^{r,0}(x), \quad \sigma_n^{r,0} = \sqrt{{}^{2p}u_n^r} \, \widehat{q}(n). \quad (3.6) $$

Remark 1. *For splines on the initial scale ($r = 0$) we retain the previous notations:* $\beta_n^p \equiv {}^p\beta_n^{0,0}$, $\gamma_n^p \equiv {}^p\gamma_n^{0,0}$, $u_n^p \equiv {}^p u_n^0$.

3.1.2 Two-scale relations

The spline space ${}^p\mathcal{S}^{r,0}$ is a subspace of ${}^p\mathcal{S}^{r-1,0}$. Therefore, the basic splines $\{\beta_n^{r,0}(x)\}$ can be expressed via the splines $\left\{\beta_l^{r-1,0}(x)\right\}$.

Theorem 3.1. *The two-scale relation*

$$ \beta_n^{r,0}(x) = a_n^{r-1,0} \beta_n^{r-1,0}(x) + a_{n+2^{-r}N}^{r-1,0} \beta_{n+2^{-r}N}^{r-1,0}(x) \quad (3.7) $$

holds for $n = 0, 1, \ldots, 2^{-r}N - 1$, *where* $a_n^{r-1,0} \triangleq 1/2 \cos^p(2^{r-1}\pi n/N)$.

Proof: By separating between even and odd terms in the Fourier series in Eq. (3.2), we get:

$$ \begin{aligned} \beta_n^{r,0}(x) &= \frac{1}{2^r} \sum_{m=-\infty}^{\infty} e^{2\pi \mathrm{i}(n/N+2^{-r+1}m)x} \left(\frac{\sin 2\pi(2^{r-1}n/N+m)}{2\pi(2^{r-1}n/N+m)} \right)^p \\ &+ \frac{1}{2^r} \sum_{m=-\infty}^{\infty} e^{2\pi \mathrm{i}((n+2^{-r}N)/N+2^{-r+1}m)x} \left(\frac{\sin 2\pi(2^{r-1}(n+2^{-r}N)/N+m)}{2\pi(2^{r-1}(n+2^{-r}N)/N+m)} \right)^p \\ &= \frac{(\cos \pi(2^{r-1}n/N))^p}{2^r} \sum_{m=-\infty}^{\infty} e^{2\pi \mathrm{i}(n/N+2^{-r+1}m)x} \left(\frac{\sin \pi(2^{r-1}n/N+m)}{\pi(2^{r-1}n/N+m)} \right)^p \\ &+ \frac{(\cos \pi(2^{r-1}(n+2^{-r}N)/N))^p}{2^r} \sum_{m=-\infty}^{\infty} e^{2\pi \mathrm{i}((n+2^{-r}N)/N+2^{-r+1}m)x} \left(\frac{\sin \pi(2^{r-1}(n+2^{-r}N)/N+m)}{\pi(2^{r-1}(n+2^{-r}N)/N+m)} \right)^p. \end{aligned} $$

Comparison between the last equation and Eq. (2.9) leads us to Eq. (3.7).■

Corollary 1. *The two-scale relation*

$$\gamma_n^{r,0}(x) = b_n^{r-1,0}\gamma_n^{r-1,0}(x) + b_{n+2^{-r}N}^{r-1,0}\gamma_{n+2^{-r}N}^{r-1,0}(x), \quad b_n^{r-1,0} \triangleq \sqrt{\frac{{}^{2p}u_n^{r-1}}{2\ {}^{2p}u_n^r}}\ \cos^p\left(\frac{2^{r-1}\pi n}{N}\right) \tag{3.8}$$

for the normalized exponential splines holds for $n = 0, 1, \ldots, 2^{-r}N - 1$.

The norms of the splines $\gamma_n^{r,0}$ and $\gamma_n^{r-1,0}$ are equal to one. Hence, we have

$$\left(b_n^{r-1,0}\right)^2 + \left(b_{n+2^{-r}N}^{r-1,0}\right)^2 = 1, \quad n = 0, 1, \ldots, 2^{-r}N - 1. \tag{3.9}$$

Denote by ${}^p\mathcal{S}^{r,1}$ the orthogonal complement to ${}^p\mathcal{S}^{r,0}$ in the space ${}^p\mathcal{S}^{r-1,0}$. We construct an orthonormal basis that characterizes ${}^p\mathcal{S}^{r,1}$. Define the splines

$$\begin{aligned}
&\gamma_n^{r,1}(x) = b_n^{r-1,1}\gamma_n^{r-1,0}(x) + b_{n+2^{-r}N}^{r-1,1}\gamma_{n+2^{-r}N}^{r-1,0}(x), \\
&b_n^{r-1,1} \triangleq \omega^{2^{r-1}n} b_{n+2^{-r}N}^{r-1,0} = \omega^{2^{r-1}n}\sqrt{\frac{{}^{2p}u_{n+2^{-r}N}^{r-1}}{2\ {}^{2p}u_n^r}}\sin^p\left(\frac{2^{r-1}\pi n}{N}\right)
\end{aligned} \tag{3.10}$$

Proposition 3.1. *The set of splines* $\{\gamma_n^{r,1}(x)\}_{n=0}^{2^{-r}N-1}$ *forms an orthonormal basis for* ${}^p\mathcal{S}^{r,1}$.

Proof: The orthogonality of the splines $\{\gamma_n^{r-1,0}(x)\}_{n=0}^{N/2^{r-1}-1}$ results in the orthogonality of $\gamma_n^{r,1}(x)$ to $\gamma_l^{r,0}(x) \in {}^p\mathcal{S}^{r,0}$ and to $\gamma_l^{r,1}(x) \in {}^p\mathcal{S}^{r,1}$, for all $l \neq n$. Due to Eq. (3.9), the squared norms $\|\gamma_n^{r,1}\|^2 = \left(b_{n+2^{-r}N}^{r,0}\right)^2 + \left(b_n^{r,0}\right)^2 = 1$. It remains to establish the orthogonality relation between $\gamma_n^{r,1}(x)$ and $\gamma_n^{r,0}(x)$. From Eqs. (3.8) and (3.10), we have:

$$\left\langle \gamma_n^{r,1}\, \gamma_n^{r,0} \right\rangle = b_n^{r-1,1}\, b_n^{r-1,0} + b_{n+2^{-r}N}^{r-1,1}\, b_{n+2^{-r}N}^{r-1,0} = \omega^{2^{r-1}n}\left(b_{n+2^{-r}N}^{r-1,0}\, b_n^{r-1,0} - b_{n+2^{-r}N}^{r-1,0}\, b_n^{r-1,0}\right) = 0. \tag{3.11}$$

■

Proposition 3.2. *The splines* $\gamma_n^{r,l}(x)$ *are the eigenvectors of the shift operator*

$$\gamma_n^{r,l}(x + 2^r k) = \omega^{2^r nk}\, \gamma_n^{r,l}(x), \quad d = 0, \ldots, 2^{-r}N - 1. \tag{3.12}$$

Proof: At the initial scale, we have from Eq. (2.16) that $\gamma_n^{0,0}(x + k) = \omega^{kn}\, \gamma_n^{0,0}(x)$. At the first scale for $l = 0, 1$

$$\gamma_n^{1,l}(x + 2k) = b_n^{1,l}\gamma_n^{0,0}(x + 2k) + b_{n+N/2}^{1,l}\gamma_{n+N/2}^{0,0}(x + 2k) = \omega^{2kn}\, \gamma_n^{1,l}(x).$$

For $r > 1$, Eq. (3.12) is derived by induction. ■

Note that the union $\{\gamma_n^{r,0}(x)\} \bigcup \{\gamma_n^{r,1}(x)\}$, $n = 0, \ldots, 2^{-r}N - 1$, forms an orthonormal basis for the entire space ${}^p\mathcal{S}^{r-1,0}$.

3.1.3 Refined split of the spline space into orthogonal subspaces

The spline space ${}^p\mathcal{S}^{r-1,0}$ is split into the orthogonal sum ${}^p\mathcal{S}^{r-1,0} = {}^p\mathcal{S}^{r,0} \bigoplus {}^p\mathcal{S}^{r,1}$. If $r > 1$, we can apply a similar procedure to the space ${}^p\mathcal{S}^{r-1,1}$. As a result, we get the decomposition ${}^p\mathcal{S}^{r-1,1} = {}^p\mathcal{S}^{r,2} \bigoplus {}^p\mathcal{S}^{r,3}$. In general, the space ${}^p\mathcal{S}^{r-1,l}$ is decomposed into the orthogonal sum ${}^p\mathcal{S}^{r-1,l} = {}^p\mathcal{S}^{r,2l} \bigoplus {}^p\mathcal{S}^{r,2l+1}$ by the following procedure. Assume that the set of exponential splines $\left\{\gamma_n^{r-1,l}(x)\right\}_n^{N/2^{r-1}-1}$ forms an orthonormal basis of the space ${}^p\mathcal{S}^{r-1,l}$. We construct a new orthonormal basis that consists of two different blocks, which are orthogonal to each other, using the coefficients $b_n^{r-1,0}$ and $b_n^{r-1,1}$ defined in Eqs. (3.8) and (3.10).

Define two sets of orthonormal splines using the coefficients $b_n^{r-1,l}$ defined in Eqs. (3.8) and (3.10):

$$\gamma_n^{r,2l+m}(x) = b_n^{r-1,m}\,\gamma_n^{r-1,l}(x) + b_{n+2^{-r}N}^{r-1,m}\,\gamma_{n+2^{-r}N}^{r-1,l}(x), \quad m = 0, 1, \quad n = 0, \ldots, 2^{-r}N - 1. \tag{3.13}$$

Denote by ${}^p\mathcal{S}^{r,2l}$ and ${}^p\mathcal{S}^{r,2l+1}$ the linear spans of the orthonormal systems $\left\{\gamma_n^{r,2l}(x)\right\}_{n=0}^{2^{-r}N-1}$ and $\left\{\gamma_n^{r,2l+1}(x)\right\}_{n=0}^{2^{-r}N-1}$, respectively. Their mutual orthogonality is established similarly to Proposition 3.1. Thus, ${}^p\mathcal{S}^{r-1,l} = {}^p\mathcal{S}^{r,2l} \bigoplus {}^p\mathcal{S}^{r,2l+1}$ and the union $\left\{\gamma_n^{r,2l}(x)\right\} \bigcup \left\{\gamma_n^{r,2l+1}(x)\right\}$, $n = 0, \ldots, 2^{-r}N-1$, forms its orthonormal basis.

Consequently, the spline space ${}^p\mathcal{S}$ can be decomposed into a series of orthogonal sums

$${}^p\mathcal{S} = {}^p\mathcal{S}^{1,0} \bigoplus {}^p\mathcal{S}^{1,1} = {}^p\mathcal{S}^{2,0} \bigoplus {}^p\mathcal{S}^{2,1} \bigoplus {}^p\mathcal{S}^{2,2} \bigoplus {}^p\mathcal{S}^{2,3} = \ldots = \bigoplus_{l=0}^{2^r-1} {}^p\mathcal{S}^{r,l}. \tag{3.14}$$

3.1.4 Upgrade of the spline's coordinates

Assume that $S(x) \in {}^p\mathcal{S}^{r,2l+m} \subset {}^p\mathcal{S}^{r-1,l}$, $m = 0, 1$, is represented by

$$S\left(x\right) = \sqrt{\frac{2^r}{N}} \sum_{n=0}^{N/2^r-1} \sigma_n^{r,2l+m} \gamma_n^{r-1,2l+m}(x). \tag{3.15}$$

Then, Eq. (3.13) implies that

$$\begin{aligned} S\left(x\right) &= \sqrt{\frac{2^r}{N}} \sum_{n=0}^{N/2^r-1} \sigma_n^{r,2l+m} \left(\gamma_n^{r-1,l}(x)\ b_n^{r-1,m} + \gamma_{n+2^{-r}N}^{r-1,l}(x)\, b_{n+2^{-r}N}^{r-1,m}\right) \\ &= \sqrt{\frac{2^r}{N}} \sum_{n=0}^{N/2^{r-1}-1} \gamma_n^{r-1,l}(x)\, \sigma_n^{r,2l+m}\, b_n^{r-1,m}. \end{aligned}$$

Hence, the coordinates of $S(x) \in {}^p\mathcal{S}^{r,2l+m}$, $m = 0, 1$, in the parent space ${}^p\mathcal{S}^{r-1,l}$ are

$$\sigma_n^{r-1,l} = \sqrt{2}\sigma_n^{r,2l+m}\, b_n^{r-1,m} \tag{3.16}$$

where $b_n^{r-1,m}$ are defined in Eqs. (3.8) and (3.10). Recall that $\sigma_n^{r,2l+m}$ is $N/2^r$-periodic.

Subsequent iteration of the relation (3.16) provides the coordinates $\{\sigma_n(x)\}$, $n = 0, \dots N-1$, of the spline $S(x) \in {}^p\mathcal{S}^{r,2l+m}$ with respect to the orthonormal basis $\{\gamma_n(x)\}$ of the initial space ${}^p\mathcal{S}$, which constitutes the SHA-spectrum of the spline.

3.2 Wavelet packets

3.2.1 Definition of spline wavelet packets

The complex-valued basis splines $\gamma_n^{r,l}(x)$ are well localized in the frequency domain but their supports in the time domain occupy the whole interval $[0, N)$ (up to periodization). We introduce a family of orthonormal bases for the spline space ${}^p\mathcal{S}$, whose elements are real-valued and localized in the time domain. Denote

$$\psi^{r,l}(x) \triangleq \sqrt{\frac{2^r}{N}} \sum_{n=0}^{N/2^r-1} \gamma_n^{r,l}(x) \in {}^p\mathcal{S}^{r,l}. \tag{3.17}$$

Proposition 3.3. *Translations* $\left\{\psi^{r,l}(x - 2^r k)\right\}$, $k = 0, \dots, N/2^r - 1$, *of the splines* $\psi^{r,l}(x)$ *form an orthonormal basis for* ${}^p\mathcal{S}^{r,l}$. *The translations* $\left\{\psi^{r,l}(x - 2^r k)\right\}$, $l = 0, \dots, 2^r - 1$, $k = 0, \dots, N/2^r - 1$, *form an orthonormal basis for the entire space* ${}^p\mathcal{S}$.

Proof: The spline $\psi^{r,l}(x - 2^r k)$ is orthogonal to any spline $\psi^{r,\tilde{l}}\left(x - 2^r \tilde{k}\right)$, for $\tilde{l} \neq l$. This is true because they belong to mutually orthogonal subspaces. The inner product of two splines from the same subspace is

$$\int_0^N \psi^{r,l}(x - 2^r k)\, \overline{\psi^{r,l}}\left(x - 2^r \tilde{k}\right) dx = \frac{2^r}{N} \sum_{n,\tilde{n}=0}^{N/2^r-1} \omega^{-2^r(kn-\tilde{k}\tilde{n})} \int_0^N \gamma_n^{r,l}(x)\, \overline{\gamma_{\tilde{n}}^{r,l}}(x)\, dx$$

$$= \frac{2^r}{N} \sum_{n=0}^{N/2^r-1} w^{-2^r n(k-\tilde{k})} = \delta_k^{\tilde{k}}, \quad k = 0, \dots, N/2^r - 1.$$

■

The splines $\{\psi^{r,0}(x)\}$ and $\{\psi^{r,1}(x)\}$ are periodic Battle-Lemarié father and mother wavelets [7, 18], respectively. The splines $\left\{\psi^{r,l}(x)\right\}$ with arbitrary $l = 0, 1, \dots, 2^r - 1$, are periodic orthonormal wavelet packets.

3.2.2 The SHA spectra of spline wavelet packets

All the spaces ${}^p\mathcal{S}^{r,l} \subset {}^p\mathcal{S}$, thus, the wavelet packets belong to the initial spline space ${}^p\mathcal{S}^{0,0}$. To operate them, we need to know the SHA spectra $\left\{\nu_n^{r,l}\right\}_{n=0}^{N-1}$ of these wavelet packets that are their coordinates in the orthonormal basis $\{\gamma_n(x)\}$, $n = 0, ..., N-1$, of the space ${}^p\mathcal{S}$.

At the initial scale we have $\psi^{0,0}(x) = N^{-1/2}\sum_{n=0}^{N-1}\gamma_n(x) \Longrightarrow \nu_n^{0,0} = 1$.

When $r > 0$, we derive the spectra using Eqs. (3.16), (3.8) and (3.10).

Wavelet packets from the first scale: For $m = 0, 1$, ${}^p\psi^{1,m}(x) = N^{-1/2}\sum_{n=0}^{N-1}\nu_n^{1,m}\gamma_n(x)$, where

$$\nu_n^{1,0} = \sqrt{2}b_n^{0,0} = \sqrt{\frac{{}^{2p}u_n^0}{{}^{2p}u_n^1}}\,\cos^p\left(\frac{\pi n}{N}\right), \quad \nu_n^{1,1} = \sqrt{2}b_n^{1,1} = \omega^n\sqrt{\frac{{}^{2p}u_{n+N/2}^0}{{}^{2p}u_n^1}}\,\sin^p\left(\frac{\pi n}{N}\right).$$

Wavelet packets from the second scale: For $m = 0, 1, 2, 3$, ${}^p\psi^{1,l}(x) = N^{-1/2}\sum_{n=0}^{N-1}\nu_n^{2,m}\gamma_n(x)$, where

$$\begin{aligned}
\nu_n^{2,0} &= \sqrt{2}b_n^{2,0}\nu_n^{1,0} = \sqrt{\frac{{}^{2p}u_n^1}{{}^{2p}u_n^2}}\cos^p\left(\frac{2\pi n}{N}\right)\nu_n^{1,0} = \sqrt{\frac{{}^{2p}u_n^0}{{}^{2p}u_n^2}}\cos^p\left(\frac{\pi n}{N}\right)\cos^p\left(\frac{2\pi n}{N}\right),\\
\nu_n^{2,1} &= \omega^{2n}\sqrt{\frac{{}^{2p}u_n^0}{{}^{2p}u_n^1}\frac{{}^{2p}u_{n+N/4}^1}{{}^{2p}u_n^2}}\,\cos^p\left(\frac{\pi n}{N}\right)\sin^p\left(\frac{2\pi n}{N}\right),\\
\nu_n^{2,2} &= \omega^n\sqrt{\frac{{}^{2p}u_{n+N/2}^0}{{}^{2p}u_n^2}}\,\sin^p\left(\frac{\pi n}{N}\right)\cos^p\left(\frac{2\pi n}{N}\right),\\
\nu_n^{2,3} &= \omega^{3n}\sqrt{\frac{{}^{2p}u_{n+N/2}^0}{{}^{2p}u_n^1}\frac{{}^{2p}u_{n+N/4}^1}{{}^{2p}u_n^2}}\,\sin^p\left(\frac{\pi n}{N}\right)\sin^p\left(\frac{2\pi n}{N}\right).
\end{aligned}$$

Similarly, the SHA spectra of the wavelet packets from the lower resolution scales are derived.

3.2.3 Structure of the SHA spectra of spline wavelet packets

Since the γ-SHA spectra $\{\sigma_n\}_{n=0}^{N-1}$ of splines are the DFT of real sequences of the B-splines coefficients, then the sequence $\{|\sigma_n|\}_{n=0}^{N-1}$ are symmetric about $N/2 - 1/2$. Therefore, it is sufficient to consider the spectra only for $n = 0, ..., N/2 - 1$.

The coefficients of the wavelet packets of the initial scale are all 1. From Eqs. (2.10) and (3.3), the coefficients are

$$2^{-1/2}\nu_n^{1,0} = \frac{\sin^p(\pi n/N)\ (2\pi(n/N))^p}{\sin^p(2\pi n/N)\ (2\pi(n/N))^p}\cos^p\left(\frac{\pi n}{N}\right)(1 + O(n^{-p})).$$

Thus, it follows that $2^{-1/2}\nu_n^{1,0}$ is close to one when n is small and monotonically decays to zero when n tends to $N/4$. The higher is the order p of the splines, the closer the shape of SHA spectrum $\left\{2^{-1/2}\nu_n^{1,0}\right\}$ is to the rectangle $[0, N/4] \times [0, 1]$. We have $|\nu_n^{1,1}| = \nu_{n+N/2}^{1,0}$. Therefore, the magnitudes of the γ-SHA spectrum $\{|\nu_n^{1,0}|\}$ mirror about $N/4 - 1/2$ the spectrum $\{\nu_n^{1,0}\}$. In other words, the SHA spectra $\left\{2^{-1/2}\nu_n^{1,0}\right\}$ and $\left\{2^{-1/2}\nu_n^{1,1}\right\}$ can be interpreted as the frequency responses of the half-band low-pass and high-pass digital filters, respectively. They split the full frequency band $[0, N/2 - 1]$ into two halves.

Similarly, the γ-SHA spectra $\{2^{-1}\nu_n^{2,0}\}$ and $\{2^{-1}\nu_n^{2,1}\}$ of the wavelet packets from the second scale split the frequency band $[0, N/4-1]$ into two halves, whereas $\{2^{-1}\nu_n^{2,3}\}$ and $\{2^{-1}\nu_n^{2,2}\}$ halve the band $[N/4, N/2-1]$. The spectra of the wavelet packet coefficients from the level r constitute a 2^r-band split of the interval $[0, N/2]$.

As a result from the above construction, we have a versatile library of symmetric waveforms of different shapes, smoothness and spans. They are not compactly supported but are well localized in the time domain. Their SHA spectra are near rectangular and their supports produce a collection of different splits of the band $[-N/2, N/2]$. Since we have expansions of these waveforms in terms of the orthonormal exponential spline bases $\{\gamma_n^p(x)\}_{n=0}^{N-1}$, then the operations of convolution, differentiation, translation, finding inner products become straightforward. Therefore, it is only natural to use these waveforms to handle the deconvolution problem. The practical computational cost of these operations does not depend on the order of the involved splines. Once the solution is found, it can be explicitly calculated at any point on the real axis.

We display in Figs. 2 – 5 the wavelet packets and their SHA spectra. Figures 2 and 3 compare the wavelet packets of the first resolution scale of orders 4 and 10, respectively. These are the Battle–Lemarié wavelets. One can observe that, while the wavelets of fourth order are better localized in the time domain, the spectra of the tenth order wavelets are near rectangular. Figure 4 displays the wavelet packets of order 10 from the second resolution scale and their SHA spectra that split the frequency domain into four bands. In Fig. 5 we display the division of the frequency domain into eight bands by SHA spectra of the tenth order wavelet packets from the third resolution scale.

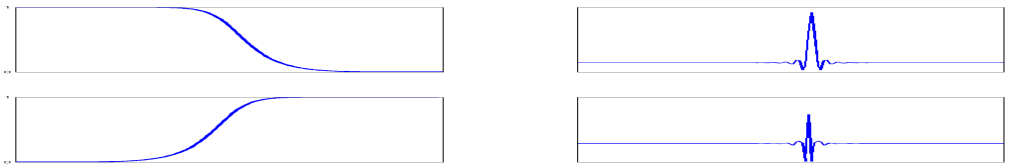

Figure 2: Right: Wavelet packets of order 4 from the first scale resolution. Left: Their SHA spectra.

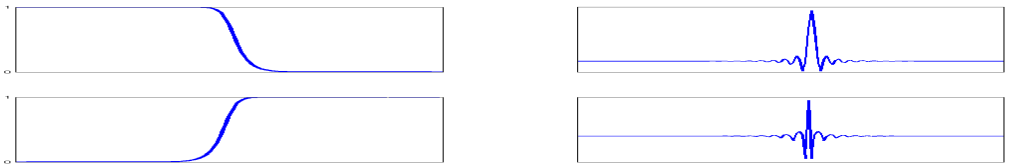

Figure 3: Right: Wavelet packets of order 10 from the first scale resolution. Left: Their SHA spectra.

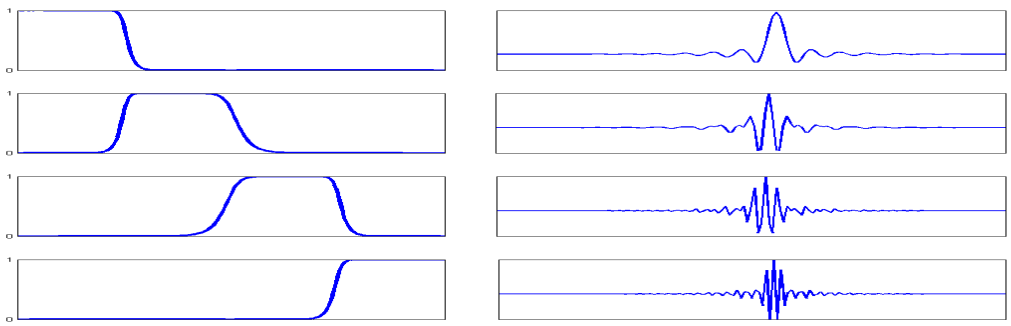

Figure 4: Right: Wavelet packets of order 10 from the second scale resolution. Left: Their SHA spectra.

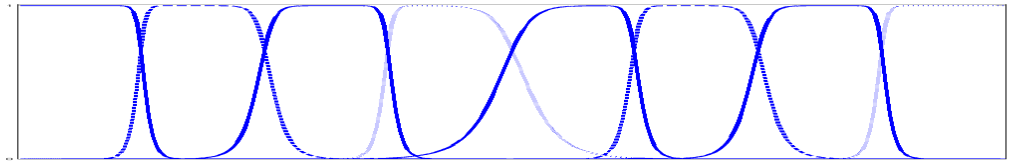

Figure 5: The SHA spectra of wavelet packets of order 10 from the third scale resolution.

4 Regularized matching pursuit (RMP) for deconvolution

The goal is to find a stable approximate solution $\tilde{f}(x)$ to the N-periodic convolution equation (Eq. (2.1)) while the data $\mathbf{z} = \{z_k\}_{k=0}^{N-1}$ and $\mathbf{h} = \{h(k)\}_{k=0}^{N-1}$ are available, $\mathbf{z} = \mathbf{g} + \mathbf{e}$, $\mathbf{g} \stackrel{\Delta}{=} \{g(k)\}$ and $\mathbf{e} \stackrel{\Delta}{=} \{e_k\}$ is a random independent identically distributed zero-mean errors array. Assume that $h(x)$ and $f(x)$ are smooth functions that belong to C^t and C^s, respectively. The Fourier spectrum of the kernel h is localized in the low-frequency area, thus, the convolution with this kernel implements low-pass filtering.

4.1 The dictionaries for RMP

We immerse the deconvolution problem into spline setting. We represent the splines via the orthonormal bases $\{\gamma_n(x)\}$. We approximate the kernel $h(x) \in C^t$ by the $q > t+1$ order spline $\chi(x) = N^{-1/2} \sum_{n=0}^{N-1} \eta_n \gamma_n^q(x) \in {}^q\mathcal{S} \subset C^t$, which interpolates the sampled kernel $\mathbf{h}$ at grid points $\{k\}$. For a successive approximation of $f \in C^s$, we use the spline wavelet packets of order $p > s+1$: $\psi^{r,l}(x) = N^{-1/2} \sum_{n=0}^{N-1} \nu_n^{r,l} \gamma_n^p(x) \in {}^p\mathcal{S}, \quad r = 0, ..., M, \ l = 0, ..., 2^m - 1$, which belong to the same space C^s. Since the available data $\mathbf{z}$ is the sampled convolution of f with the kernel h, which was corrupted by noise, it is tested by the sampled convolution splines $\theta^{r,l}(x) \stackrel{\Delta}{=} \chi \star \psi^{r,l}(x) =$

$N^{-1/2}\sum_{n=0}^{N-1}\tau_n^{r,l}\,\gamma_n^{p+q}(x)\in\ {}^{p+q}\mathcal{S}$ of order $p+q$. The coefficients are $\tau_n^{r,l}=U_n^{p,q}\eta_n\,\nu_n^{r,l}$, where $U_n^{p,q}$ is defined in Eq. (2.18).

Unlike the conventional MP, we use two different dictionaries $\mathbf{D}_A$ and $\mathbf{D}_T$ for approximation of the solution and for testing the reminders, respectively. The dictionary $\mathbf{D}_A$ is formed from one-sample translations of the spline wavelet packets $\psi^{r,l}(x)\in\ {}^{p}\mathcal{S}^{r,l}$, while the testing dictionary $\mathbf{D}_T$ from one-sample translations of the splines $\theta^{r,l}(x)\in\ {}^{p}\mathcal{S}^{r,l}$, which are sampled on the grid. Denote the N-periodic sequences by $\Theta_k^{r,l}\triangleq\left\{\Theta_k^{r,l}(i)=\theta^{r,l}(i+k)\right\},\ i=0,...,N-1$.

Thus, the spline wavelet packets constitute the dictionaries

$$\mathbf{D}_A=\left\{\psi_k^{r,l}(x)\right\}_{k=0}^{N-1},\quad \psi_k^{r,l}(x)=\psi^{r,l}(x+k)=\sqrt{\frac{1}{N}}\sum_{n}^{j}\nu_n^{r,l}\,\omega^{kn}\,\gamma_n(x), \tag{4.1}$$

$$\mathbf{D}_T=\left\{\Theta_k^{r,l}\right\}_{k=0}^{N-1},\quad \Theta_k^{r,l}(i)=\frac{1}{N}\sum_{n=0}^{N-1}\omega^{(k+i)n}\,Q_n^{p,q}\nu_n^{r,l}\,\eta_n,\quad k=0,...,N-1. \tag{4.2}$$

The sequence $Q_n^{p,q}$ is defined in Eq. (2.24).

4.2 Outline of the algorithm

In typical practical applications, the convolution kernel $h(x)$ is efficiently bandlimited. In other words, its significant Fourier coefficients $C_n(h)$ occupy a relatively narrow band around zero, $-K<n<K$, where $K<N/2$. Thus, the SHA spectrum of the interpolatory spline $\chi(x)$ is efficiently bandlimited as well. SHA spectra of the wavelet packets $\psi^{r,l}(x)$ occupy different subintervals of $-N/2<n<N/2$. Some of these subintervals have a small (if any) overlap with the support of SHA spectrum of $\chi(x)$. If $\psi^{\tilde{r},\tilde{l}}(x)$ is one of such wavelet packets then the squared norm of the corresponding convolution spline $\|\theta^{\tilde{r},\tilde{l}}\|^2=N^{-1}\sum_{n=0}^{N-1}\left|U_n^{\tilde{r},\tilde{l}}\eta_n\,\nu_n^{\tilde{r},\tilde{l}}\right|^2$ is close (or equal) to zero. In order to avoid instability of the algorithm, discard corresponding $\Theta^{\tilde{r},\tilde{l}}$ from the dictionary.

Let $\mathbf{z}^0=\mathbf{z}=\mathbf{g}+\mathbf{e}$, $f^0(x)=0$. We will test the remainders by the discrete signals $\Theta_k^{r,l}$. Assume the test signal $\mu\Theta_{\underline{k}}^{\underline{r},\underline{l}}$ fits best $\mathbf{z}^0$. Then, we put $\mathbf{z}^1=\mathbf{z}^0-\mu\Theta_{\underline{k}}^{\underline{r},\underline{l}}$, $f^1(x)=f^0(x)+\mu\psi_{\underline{k}}^{\underline{r},\underline{l}}(x)$. Then, the procedure is iterated.

4.2.1 Oblique projection

In the conventional MP scheme, the search for the best fitting dictionary element is implemented via orthogonal projection of the reminder onto the normalized dictionary elements. In our case, this approach should be modified in order to avoid instability of the solution. Recall that for all $k=0,...,N-1$, $\|\Theta_k^{r,l}\|=\sqrt{\sum_{i=0}^{N-1}\left(\theta^{r,l}(i+k)\right)^2}=\|\theta^{r,l}\|$.

The orthogonal projection of $\mathbf{z^0}$ onto the normalized $\Theta_k^{r,l}$ is

$$\mathbf{z}_k^{0,r,l} = \alpha_k^{r,l} \frac{\Theta_k^{r,l}}{\|\theta^{r,l}\|} = \mu_k^{r,l} \Theta_k^{r,l}, \quad \mu_k^{r,l} \triangleq \frac{\alpha_k^{r,l}}{\|\theta^{r,l}\|} = \frac{\left\langle \Theta_k^{r,l}, \mathbf{z}^0 \right\rangle}{\|\theta^{r,l}\|^2} = \frac{\left\langle \Theta_k^{r,l}, \mathbf{g} \right\rangle}{\|\theta^{r,l}\|^2} + \frac{\left\langle \Theta_k^{r,l}, \mathbf{e} \right\rangle}{\|\theta^{r,l}\|^2}. \tag{4.3}$$

The corresponding element from the approximation dictionary is $\mu_k^{r,l}\ \psi_k^{r,l}(x)$.

A deficient spectral overlap of the wavelet packet $\psi^{r,l}(x)$ with $\chi(x)$ results in a small norm $\|\theta^{r,l}\|$ for the testing elements. Consequently, because of the presence of the term $\left\langle \Theta_k^{r,l}, \mathbf{e} \right\rangle / \|\theta^{r,l}\|^2$ in Eq. (4.3), the coefficients $\mu_k^{r,l}$ for the approximation elements $\psi_k^{r,l}(x)$ (whose norm is equal to one) can be large. This is a reason for the solution's instability. To handle it, we replace the orthogonal projection of the reminders onto the dictionary elements by an oblique projection. To be specific, instead of $\mu_k^{r,l} = \left\langle \Theta_k^{r,l}, \mathbf{z}^0 \right\rangle / \|\Theta_k^{r,l}\|^2$, we find $\mu_k^{r,l}(\rho)$ which minimizes the function

$$J_{k,\rho}^{r,l}(\mu, \mathbf{z}^0) = \rho\mu^2 + D_k^{r,l}(\mu, \mathbf{z}^0), \quad = D_k^{r,l}(\mu, \mathbf{z}^0) \triangleq \sum_{i-0}^{N-1} \left(\mu \Theta_k^{r,l}(i) - \mu_k^{r,l}\ \Theta_k^{r,l}(i) \right)^2$$

$$= \left(\mu - \mu_k^{r,l} \right)^2 \sum_{i-0}^{N-1} \left(\Theta_k^{r,l}(i) \right)^2 = \left(\mu - \mu_k^{r,l} \right)^2 \left\| \theta^{r,l} \right\|_{l^2}^2,$$

where ρ is a numerical parameter. Hence,

$$\mu_k^{r,l}(\rho) = \frac{\mu_k^{r,l}\ \left\| \theta^{r,l} \right\|_{l^2}^2}{\rho + \|\theta^{r,l}\|_{l^2}^2} = \frac{\left\langle \Theta_k^{r,l}, \mathbf{z}^0 \right\rangle}{\rho + \|\theta^{r,l}\|_{l^2}^2}. \tag{4.4}$$

Denote

$$d_k^{r,l}(\rho) \triangleq D_k^{r,l}(\mu_k^{r,l}(\rho), \mathbf{z}^0) = \left(\frac{Z_k^{r,l}\ \rho}{\rho + \|\theta^{r,l}\|_{l^2}^2} \right)^2, \quad \text{where } Z_k^{r,l} \triangleq \frac{\left| \left\langle \Theta_k^{r,l}, \mathbf{z}^0 \right\rangle \right|}{\|\theta^{r,l}\|_{l^2}} \tag{4.5}$$

is the norm of the orthogonal projection of $\mathbf{z}^0$ onto $\Theta_k^{r,l} / \left\| \Theta_k^{r,l} \right\| = \Theta_k^{r,l} / \left\| \theta^{r,l} \right\|$. The function $\mu_k^{r,l}(\rho)$ decays monotonically from $\mu_k^{r,l}(0) = \mu_k^{r,l}$ to $\mu_k^{r,l}(\infty) = 0$. Once the value of the parameter ρ is properly selected, $\mu_k^{r,l}(\rho)$ is used as the coefficient for the solution approximation element $\psi^{r,l}(x)$. For this approximation to be stable, this coefficient should not be too large even when this is the case for $\mu_k^{r,l} = \left\langle \Theta_k^{r,l}, \mathbf{z}^0 \right\rangle / \|\theta^{r,l}\|^2$. This is achieved by increasing ρ. On the other hand, the function $d_k^{r,l}(\rho)$, which is the squared norm of deviation of the oblique $\mu_k^{r,l}(\rho)\Theta_k^{r,l}$ from the orthogonal projection $\mu_k^{r,l}\Theta_k^{r,l}$ of $\mathbf{z}^0$ onto the testing element $\Theta_k^{r,l}$, grows monotonically from $d_k^{r,l}(0) = 0$ to $d_k^{r,l}(\infty) = \left(Z_k^{r,l} \right)^2$. It does not make sense for the oblique projection to approach the orthogonal one closer than the noise level. Therefore, we can increase ρ (thus reducing $\mu_k^{r,l}(\rho)$) until

$$d_k^{r,l}(\rho) = \left(\frac{Z_k^{r,l}\ \rho}{\rho + \|\theta^{r,l}\|_{l^2}^2} \right)^2 = \left(E^{r,l} \right)^2, \quad \text{where } E^{r,l} \triangleq \frac{\left| \left\langle \Theta_k^{r,l}, \mathbf{e} \right\rangle \right|}{\|\theta^{r,l}\|_{l^2}} = \frac{\left| \left\langle \theta^{r,l}, \mathbf{e} \right\rangle \right|}{\|\theta^{r,l}\|_{l^2}} \tag{4.6}$$

is the norm of the orthogonal projection of the error vector $\mathbf{e}$ onto $\Theta_k^{r,l}/\left\|\theta^{r,l}\right\|$. The terms $E^{r,l}$ in Eq. (4.6) do not depend on the shift parameter k because the characteristics of the noise vector $\mathbf{e}$ are shift invariant. Equation (4.6) is used for the selection of the parameter ρ, provided we are able to evaluate $E^{r,l}$. Thus,

$$\rho_k^{r,l} = \frac{E^{r,l}\ \left\|\theta^{r,l}\right\|^2}{(Z^{r,l} - E^{r,l})}, \quad \mu_k^{r,l}(\rho) = \mu_k^{r,l}\left(1 - \frac{E^{r,l}}{Z^{r,l}}\right) = \frac{\left\langle \Theta_k^{r,l}, \mathbf{z}^0 \right\rangle}{\left\|\theta^{r,l}\right\|^2}\left(1 - \frac{\left|\left\langle \theta^{r,l}, \mathbf{e}\right\rangle\right|}{\left|\left\langle \Theta_k^{r,l}, \mathbf{z}^0 \right\rangle\right|}\right). \tag{4.7}$$

The oblique projection of $\mathbf{z^0}$ onto the normalized $\Theta_k^{r,l}$ is

$$\mathbf{z}_k^{0,r,l}(\rho) = \alpha_k^{r,l}(\rho)\frac{\Theta_k^{r,l}}{\left\|\theta^{r,l}\right\|}, \quad \alpha_k^{r,l}(\rho) = \left\|\theta^{r,l}\right\|\mu_k^{r,l}(\rho) = \frac{\left\langle \Theta_k^{r,l}, \mathbf{z}^0 \right\rangle}{\left\|\theta^{r,l}\right\|}\left(1 - \frac{\left|\left\langle \theta^{r,l}, \mathbf{e}\right\rangle\right|}{\left|\left\langle \Theta_k^{r,l}, \mathbf{z}^0 \right\rangle\right|}\right). \tag{4.8}$$

4.2.2 Pursuit

In order to find the dictionary element $\Theta_k^{r,l}$, which fits best the signal $\mathbf{z}^0$, we compare the magnitudes of the oblique projection coefficients $\alpha_k^{r,l}(\rho)$. Let $\underline{r}, \underline{l}, \underline{k} = \arg\max_{r,l,k}\left|\alpha_k^{r,l}(\rho)\right|$. Denote $\mu^1 \triangleq \mu_{\underline{k}}^{\underline{r},\underline{l}}(\rho)$, $\psi^1(x) \triangleq \psi_{\underline{k}}^{\underline{r},\underline{l}}(x)$ and $\Theta^1 \triangleq \Theta_{\underline{k}}^{\underline{r},\underline{l}}$. Then, we put $\mathbf{z}^1 = \mathbf{z}^0 - \mu^1\Theta_{\underline{k}}^{\underline{r},\underline{l}}$, $f^1(x) = f^0(x) + \mu^1\psi_{\underline{k}}^{\underline{r},\underline{l}}(x)$. Then, the procedure is iterated using $\mathbf{z}^1$ instead of $\mathbf{z}^0$.

It is seen from Eq. (4.8) that the oblique projection coefficients $\alpha_k^{r,l}(\rho)$ depend on shares of the coherent structure and of noise in the projection of the remainder onto the normalized testing signal $\Theta_k^{r,l}$. The bigger the noise share, the smaller is the coefficients. Subsequent pursuit steps extract pieces of coherent structure from the signal $\mathbf{z}$. Therefore, the noise share in the reminder increases and the oblique projection coefficients tend to zero. It is natural to stop the pursuit when the coefficients become sufficiently small.

4.3 Computational scheme

The SHA provides efficient tools for fast implementation of the RMP algorithm. Once we have to restore a signal or a set of signals, which are blurred by similar kernels and corrupted by white noise with the similar characteristics, some preliminary operations should be conducted.

4.3.1 Preprocessing

Dictionaries: We choose order $q \geq t+1$ of the spline $\chi(x)$, which interpolates the kernel $h(x) \in C^t$ and calculate its SHA coordinates

$$\chi(x) = N^{-1/2}\sum_{n=0}^{N-1}\eta_n\,\gamma_n^q(x) \in {}^q\mathcal{S} \subset C^t, \quad \eta_n = \frac{\hat{h}(n)}{V_n^q},$$

where the sequence V_n^q was defined in Eq. (2.17).

Basing on a prior information on the smoothness of the solution $f(x) \in C^s$, we choose the depth M and the order $p \geq s+1$ of the spline wavelet packets, which are used for the solution approximation, and calculate their SHA spectra using Eqs. (3.16), (3.8) and (3.10):

$$\psi^{r,l}(x) = \sqrt{\frac{1}{N}} \sum_{n=0}^{N-1} \nu_n^{r,l} \, \gamma_n^p(x) \in {}^p\mathcal{S} \subset C^s, \quad r = 0, ..., M, \; l = 0, ..., 2^m - 1.$$

Then, the elements $\psi_k^{r,l}(x)$ of the approximation dictionary $\mathbf{D}_A$ are given by Eq. (4.1).

From the coordinates η_n and $\nu_n^{r,l}$, we derive the elements

$$\Theta_k^{r,l} = \left\{ \Theta_k^{r,l}(i) = \frac{1}{N} \sum_{n=0}^{N-1} \omega^{(k+i)n} \, Q_n^{p,q} \nu_n^{r,l} \, \eta_n \right\}_{i=0}^{N-1} \qquad k = 0, ..., N-1,$$

of the testing dictionary $\mathbf{D}_T$. The sequence $Q_n^{p,q}$ was defined in Eq. (2.24). For all $k = 0, ..., N-1$, the norms are

$$\left\| \Theta_k^{r,l} \right\| = \left\| \theta^{r,l} \right\| = \sqrt{\sum_{i=0}^{N-1} \theta^{r,l}(i)^2} = \sqrt{\sum_{n=0}^{N-1} \left| Q_n^{p,q} \nu_n^{r,l} \, \eta_n \right|^2}.$$

Some of the norms $\left\| \theta^{r,l} \right\|$ are very close (or equal) to zero. We discard the corresponding elements $\Theta_k^{r,l}$ and $\psi_k^{r,l}(x)$ from the dictionaries. Denote the reduced approximation and testing dictionaries by $\tilde{\mathbf{D}}_A$ and $\tilde{\mathbf{D}}_T$, respectively.

Modeling the noise: We assume that the error vector $\mathbf{e}$ is a zero mean Gaussian white noise. Typically, the convolution kernel $h(x)$ is efficiently bandlimited, that is its significant Fourier coefficients $C_n(h)$ occupy a relatively narrow band around zero, $-K < n < K$, where $K < N/2$. Hence, the FFT coefficients of the data vector $\mathbf{z}$ $\{\hat{z}(n)\}_{n \in [K, N/2-1] \cup [-N/2, -K]} \approx \{\hat{e}(n)\}_{n \in [K, N/2-1] \cup [-N/2, -K]}$. Relying on the fact that the power spectrum , $\{|\hat{e}(n)|^2\}$ of the white noise $\mathbf{e}$ is close to a constant for all $n = -N/2, ..., N/2-1$, we evaluate the variance

$$\sigma^2 \approx \frac{1}{(N-K)^2} \sum_{n \in [K, N/2-1] \cup [-N/2, -K]} |\hat{z}(n)|^2 . \tag{4.9}$$

We model the noise vector as a zero mean Gaussian random process $\tilde{\mathbf{e}} = \{\tilde{e}_i\}_{i=0}^{N-1}$, whose variance is σ^2.

Let $\left\{ \widehat{\tilde{e}}(n) \right\}_{n=0}^{N-1}$ be the FFT spectrum of the model vector $\tilde{\mathbf{e}}$. Then, we estimate the values $\left| \left\langle \theta^{r,l}, \mathbf{e} \right\rangle \right|$, which are needed for the oblique projections (4.8), as

$$\left| \left\langle \theta^{r,l}, \mathbf{e} \right\rangle \right| \approx e^{r,l} \triangleq \left| \left\langle \theta^{r,l}, \tilde{\mathbf{e}} \right\rangle \right| = \frac{1}{N} \left| \sum_{n=0}^{N-1} Q_n^{p,q} \nu_n^{r,l} \, \eta_n \, \overline{\widehat{\tilde{e}}}(n) \right| . \tag{4.10}$$

Remark 4.1. *To make the estimation in Eq. (4.10) robust, it is advisable to calculate* $\left\langle \theta^{r,l}, \tilde{\mathbf{e}} \right\rangle$ *several times using different realizations of the random process* $\tilde{\mathbf{e}}$ *and to average the results.*

Initialization of the algorithm: We approximate the solution $f(x)$ of Eq. (2.1) by a sequence of splines $f^j(x) = N^{-1/2} \sum_{n=0}^{N-1} \sigma_n^j \, \gamma_n(x) \in {}^p\mathcal{S}$, which are combinations of the wavelet packets from the reduced dictionary $\tilde{\mathbf{D}}_A$.

1. Put $f^0(x) \equiv 0 \Longleftrightarrow \sigma_n^0 = 0 \; \forall k$, $\mathbf{z}^0 = \mathbf{z} \Longleftrightarrow \hat{z}^0(n) = \hat{z}(n), \; n = 0, ..., N-1$.
2. Calculate the inner products
$$T_k^{r,l}(\mathbf{z}^0) \triangleq \left\langle \Theta_k^{r,l}, \mathbf{z}^0 \right\rangle = \frac{1}{N} \sum_{n=0}^{N-1} \omega^{kn} \, Q_n^{p,q} \nu_n^{r,l} \, \eta_n \, \overline{\hat{z}^0}(n).$$
3. Calculate the oblique projection coefficients
$$\alpha_k^{r,l}(\mathbf{z}^0) \triangleq \frac{T_k^{r,l}(\mathbf{z}^0)}{\|\theta^{r,l}\|} \left(1 - \frac{e^{r,l}}{\left| T_k^{r,l}(\mathbf{z}^0) \right|} \right),$$
where $e^{r,l}$ is defined in Eq. (4.10).
4. Set a small threshold R_s for the stopping rule, for example, $\max \left| \alpha_k^{r,l}(\mathbf{z}^0) \right| / 100$.
5. $j = 0$.

4.3.2 Pursuit

1. Find $\underline{r}, \underline{l}, \underline{k} = \arg\max_{r,l,k} \left| \alpha_k^{r,l}(\mathbf{z}^j) \right|$.
2. If $\left| \alpha_{\underline{k}}^{\underline{r},\underline{l}} \right| > R_s$:
   - Denote $\mu^{j+1} \triangleq \alpha_{\underline{k}}^{\underline{r},\underline{l}} / \left\| \theta^{\underline{r},\underline{l}} \right\|$.
   - Put $\sigma_n^{j+1} = \sigma_n^j + \mu^{j+1} \nu_n^{\underline{r},\underline{l}} \, \omega^{\underline{k}n}, \; n = 0, ..., N-1$.
   - Put $\hat{z}^{j+1}(n) = \hat{z}^j(n) - \mu^{j+1} \, Q_n^{p,q} \, \eta_n \, \nu_n^{\underline{r},\underline{l}} \, \omega^{\underline{k}n}, \; n = 0, ..., N-1$.
   - Calculate the inner products
$$T_k^{r,l}(\mathbf{z}^{j+1}) = \frac{1}{N} \sum_{n=0}^{N-1} \omega^{kn} \, Q_n^{p,q} \nu_n^{r,l} \, \eta_n \, \overline{\hat{z}^{j+1}}(n).$$
   - Calculate the oblique projection coefficients
$$\alpha_k^{r,l}(\mathbf{z}^{j+1}) = \frac{T_k^{r,l}(\mathbf{z}^{j+1})}{\|\theta^{r,l}\|} \left(1 - \frac{e^{r,l}}{\left| T_k^{r,l}(\mathbf{z}^{j+1}) \right|} \right).$$

- $j = j + 1$, go to 1.

3. Otherwise: the solution $f(x) \approx f^j(x) = N^{-1/2} \sum_{n=0}^{N-1} \sigma_n^j \, \gamma_n(x)$.

Remark 4.2. *The described algorithm can be utilized for restoration of signals, which are corrupted by noise (no blurring). For this, the testing dictionary $\boldsymbol{D}_T$ defined in Eq. (4.3) should be replaced by*

$$\boldsymbol{D}_T = \left\{ \psi_k^{r,l} \right\}_{k=0}^{N-1}, \quad \psi_k^{r,l}(i) = \frac{1}{N} \sum_{n=0}^{N-1} \omega^{(k+i)n} \, \nu_n^{r,l}, \quad k = 0, ..., N-1.$$

5 Experimental results

We conducted a series of experiments to test the deconvolution algorithm that was applied to blurred natural signals, which were affected by a Gaussian white noise. We managed to successfully approximate the original signals even when blurring and noise were strong. As a source for the test signals we used the benchmark images such as Barbara, Lena, Boats and fingerprint, where each column was processed separately. Once the stopping threshold R_s was defined (it was the same for all the experiments), the number of iterations for each signal (column) was determined automatically. Typically, separate processing 512 columns of length 512 required 1 to 1.5 minutes in Matlab environment depending on the strength of the blurring. Strong blurring means that the effective bandwidth of the kernel's spectrum (the passband of the filter) is narrow. Thus, the reduced dictionaries $\tilde{\mathbf{D}}_A$ and $\tilde{\mathbf{D}}_T$ contain relatively small number of waveforms. In this case, processing is faster compared to the case when blurring is weak. We compared the results of application of the MP algorithm with the results derived from application of the conventional Tikhonov regularization (TRA) and Wiener (WA) deconvolution algorithms (Matlab functions `deconvreg` and `deconvwnr`, respectively.) We evaluate the quality of images restoration visually and by the peak signal to noise ratio (PSNR) in decibels

$$PSNR \triangleq 10 \log_{10} \left(\frac{N \, M^2}{\sum_{k=1}^{N} (x_k - \tilde{x}_k)^2} \right) \, dB.$$

Here, $\{x_k\}_{k=1}^N$ are the samples of the original image and $M = \max_k |x_k|$, while $\{\tilde{x}_k\}_{k=1}^N$ are the samples of the restored image. In addition, we observe restoration of separate columns.

Example Bmbsn - Barbara with moderate blurring and strong noise: In this experiment, columns of the Barbara image (Fig. 6) were blurred using Gaussian kernel whose STD $\sigma_k = 3$ and corrupted by Gaussian white noise whose STD was $\sigma_n = 20$. We display in Fig. 7 the blurring kernel and its Fourier spectrum, which is effectively confined within the band [-100, 100].

Figure 6: **Bmbsn** example: Barbara.

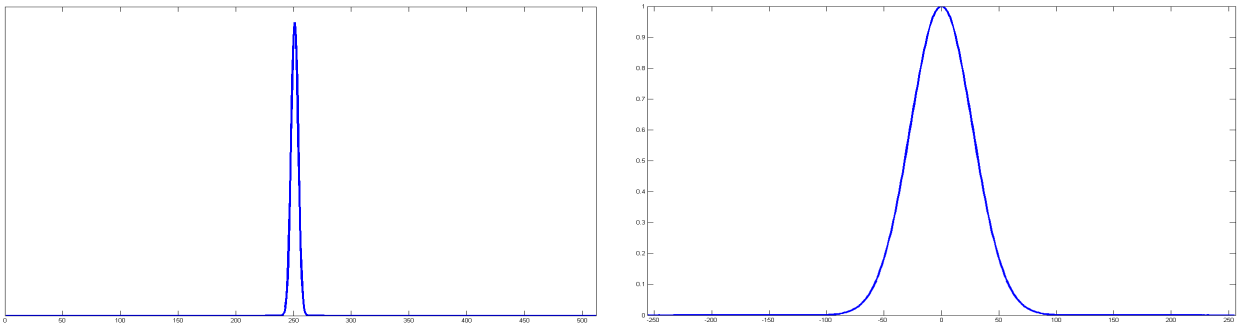

Figure 7: **Bmbsn** example. Left: The convolving kernel (STD=3). Right: Its Fourier spectrum.

Figure 8 displays the image whose columns are blurred and corrupted by noise and its restoration by different deconvolutionmethods.

Figure 8: **Bmbsn** example. Top left: blurred noised image. Top right: image restored by MP. Bottom left: image restored by TRA. Top right: image restored by WA. The spline wavelet packets of fourth order from scales 2 to 6 were used.

The PSNR values are given in Table 1.

Input image	MP rest.	TRA rest.	WA rest.
24.8576	**26.4249**	25.3293	25.6639

Table 1: **Bmbsn** example. PSNR values

The left figure in Fig. 9 depicts the numbers $I(k)$ of the pursuit iterations for each of the 512 columns. These numbers vary from 100 to 170. This means that the k-th column is represented by $I(k)$ waveforms. The right figure illustrates a typical behavior of the projection coefficients $\alpha_{\underline{k}}^{r,l}$ with respect to the iterations. We see that after 70 iterations, the coefficients actually become to zero. It is a good reason to stop the pursuit.

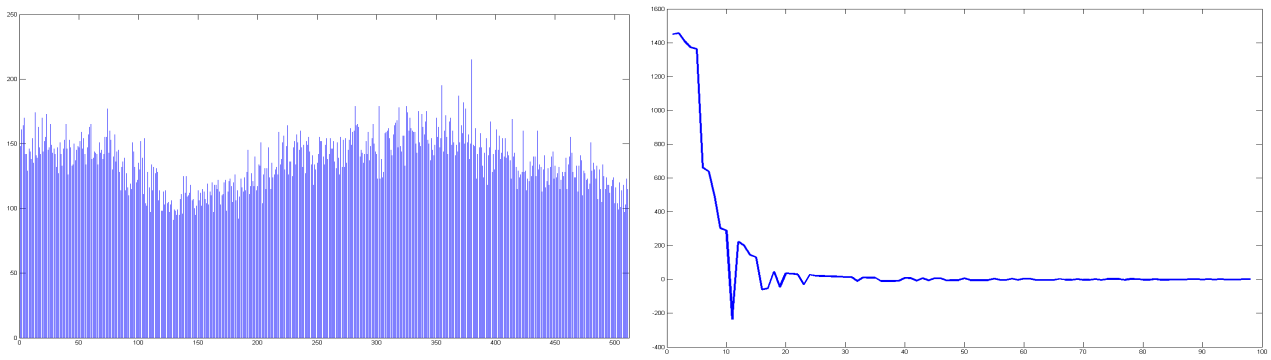

Figure 9: **Bmbsn** example. Left: Numbers of the pursuit iterations for each of the 512 columns. X – indices of columns, Y – numbers of iterations. Right: behavior of the projection coefficients $\alpha^{r,l}_{\underline{k}}$. X – number of iterations, Y – $\alpha^{r,l}_{\underline{k}}$.

Figures 10 and 11 display restoration of column 30 and column 450, respectively.

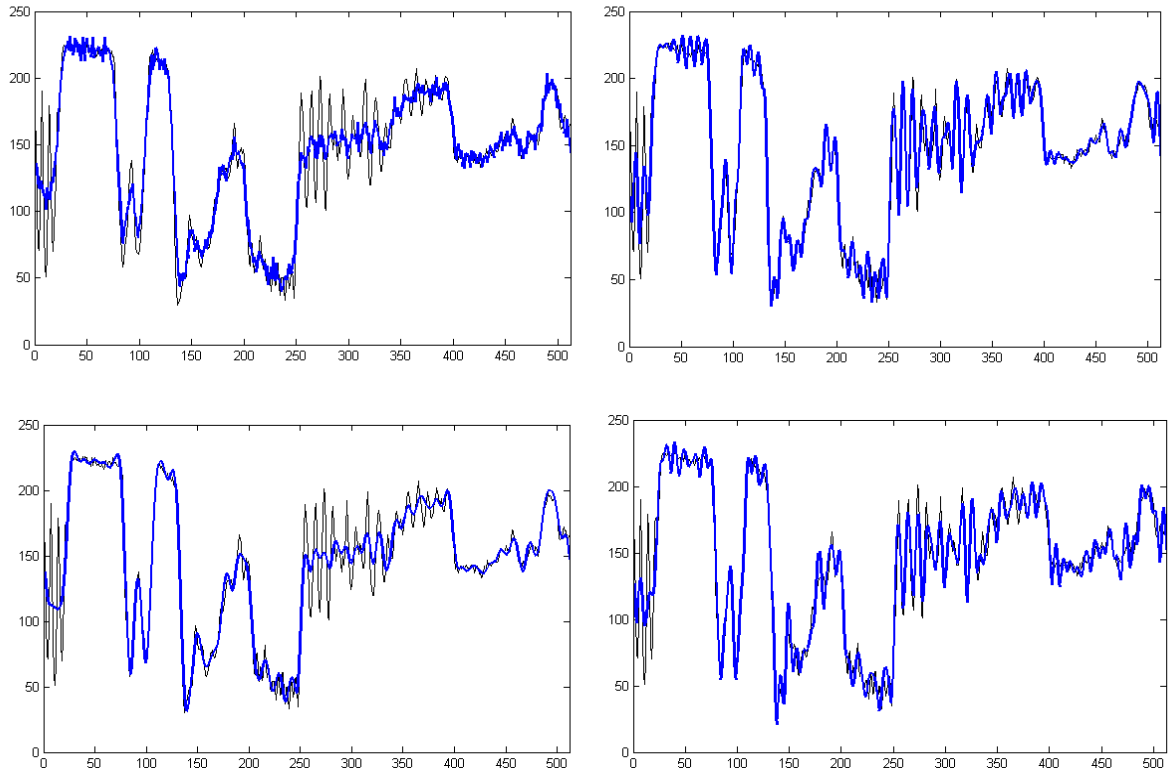

Figure 10: **Bmbsn** example. Top left: blurred noised column 30. Top right: column 30 restored by MP. Bottom left: column 30 restored by TRA. Top right: column 30 restored by WA. The thin line in all the figures depicts the original signal.

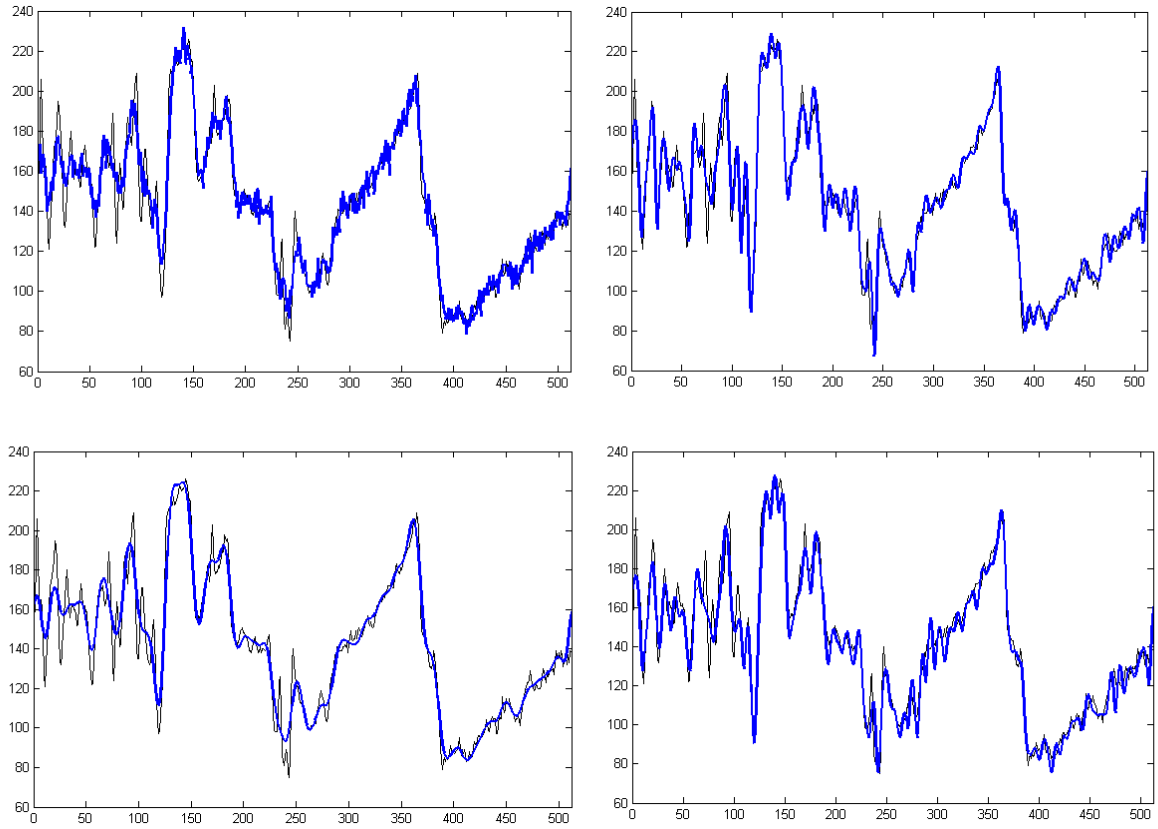

Figure 11: **Bmbsn** example. Top left: blurred noised column 450. Top right: column 450 restored by MP. Bottom left: column 450 restored by TRA. Top right: column 450 restored by WA. The thin line in all the figures depicts the original signal.

Observations:

1. The highest PSNR is produced by the MP restoration of columns. It exceeds the WA PSNR by 0.76 dB.
2. Visually, the best restoration of the image texture is achieved by the MP restoration of columns.
3. Comparing restoration of column 30 and of column 450 by different algorithms, we observe that MP provides almost perfect restoration of the curves while WA and, especially, TRA miss some events.

Lsbmn example - Lena with strong blurring and moderate noise: In this experiment, columns of the Lena image (Fig. 12) were blurred using Gaussian kernel whose STD was $\sigma_k = 4$ and corrupted by Gaussian white noise whose STD was $\sigma_n = 4$.

Figure 12: **Lsbmn** example: Lena.

Figure 13 displays the image whose columns are blurred and corrupted by noise and its restoration by different deconvolutionmethods.

Figure 13: **Lsbmn** example. Top left: blurred noised image. Top right: image restored by MP. Bottom left: image restored by TRA. Top right: image restored by WA. The spline wavelet packets of fourth order from scales 2 to 6 were used.

The PSNR values are given in Table 2.

Input image	MP rest.	TRA rest.	WA rest.
28.0639	**30.3694**	29.6711	29.4488

Table 2: **Lsbmn** example. example. PSNR values

Figures **??** and 15 display the restoration of column 300 and column 250, respectively.

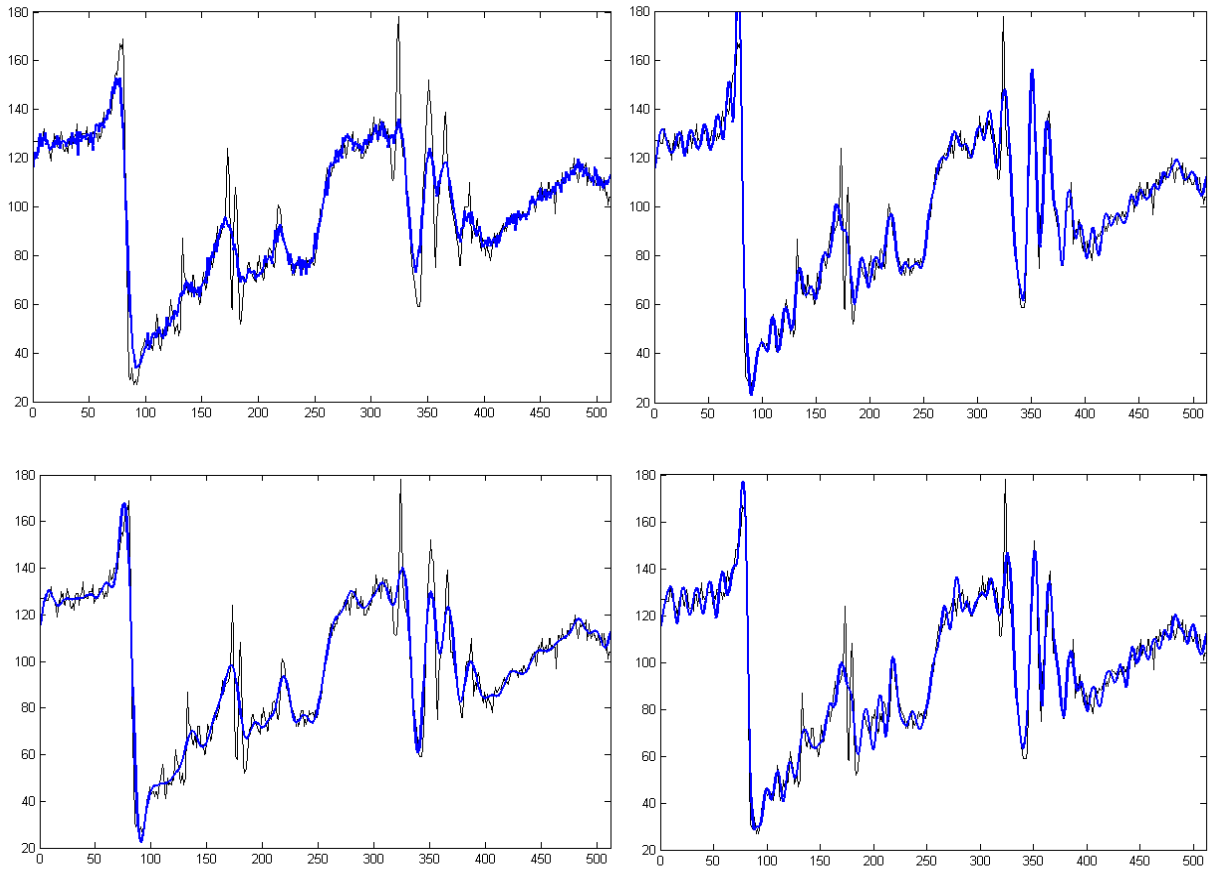

Figure 14: **Lsbmn** example. Top left: blurred noised column 300. Top right: column 30 restored by MP. Bottom left: column 300 restored by TRA. Top right: column 300 restored by WA. The thin line in all the figures depicts the original signal.

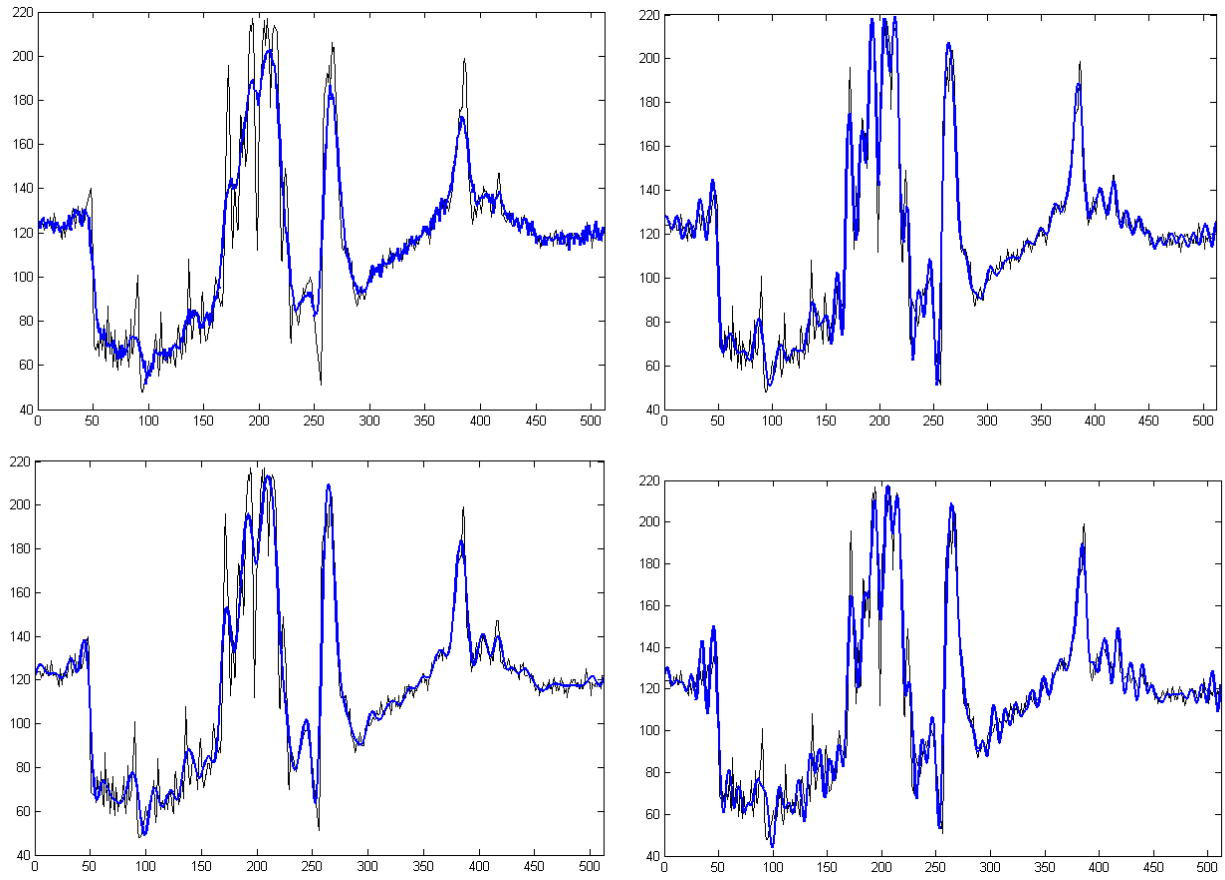

Figure 15: **Lsbmn** example. Top left: blurred noised column 250. Top right: column 250 restored by MP. Bottom left: column 250 restored by TRA. Top right: column 250 restored by WA. The thin line in all the figures depicts the original signal.

Observations:

1. The highest PSNR is produced by the MP restoration of columns. It exceeds the TRA PSNR by 0.7 dB.
2. Visually, the best restoration of the image texture is achieved by the MP restoration of columns. The image restored by MP looks smoother compared to other images while practically all details are restored in spite of strong blurring of the input image.
3. Comparing restoration of column 300 and of column 250 by different algorithms, we observe that MP provides restoration of the curves very close to the original while WA produces oscillating artifacts and TRA is oversmoothed.

Fmbmn example - Fingerprint with moderate blurring and moderate noise: In this experiment, the columns of the Fingerpint image (Fig. 20) were blurred using Gaussian kernel

whose STD was $\sigma_k = 3$ and corrupted by Gaussian white noise whose STD was $\sigma_n = 3$. The image consists of fine texture, most of which is lost in the input image.

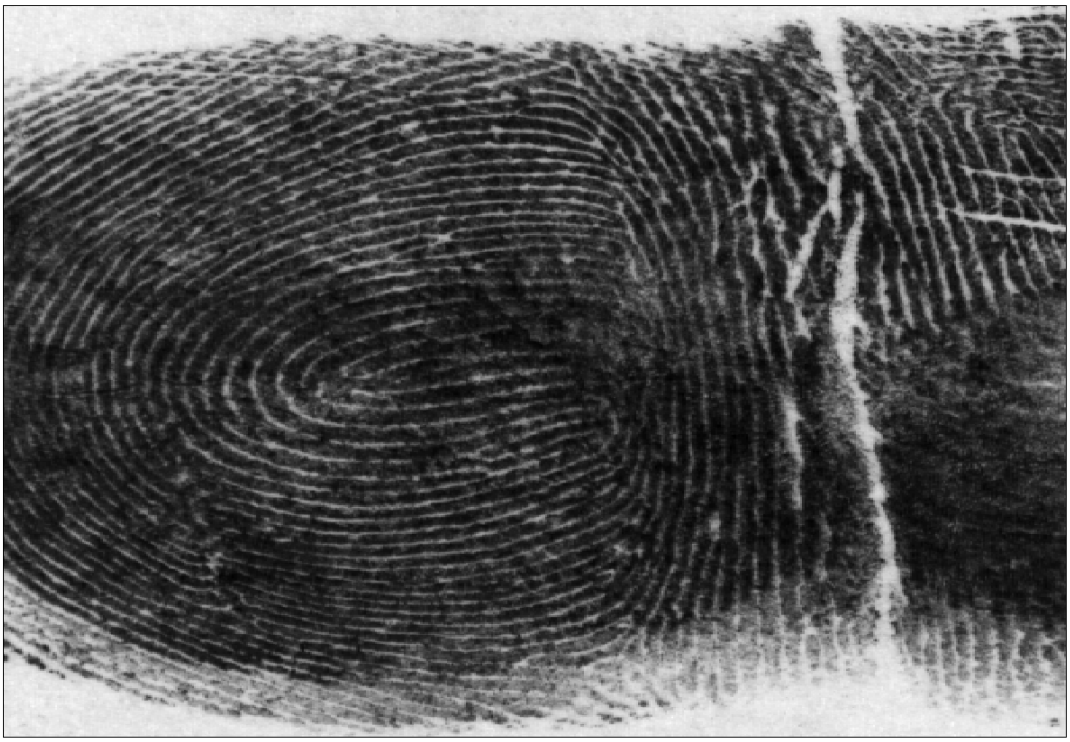

Figure 16: **Fmbmn** example: Fingerpint.

Figure 17 displays the image whose columns are blurred and corrupted by noise and its restoration by different deconvolutionmethods.

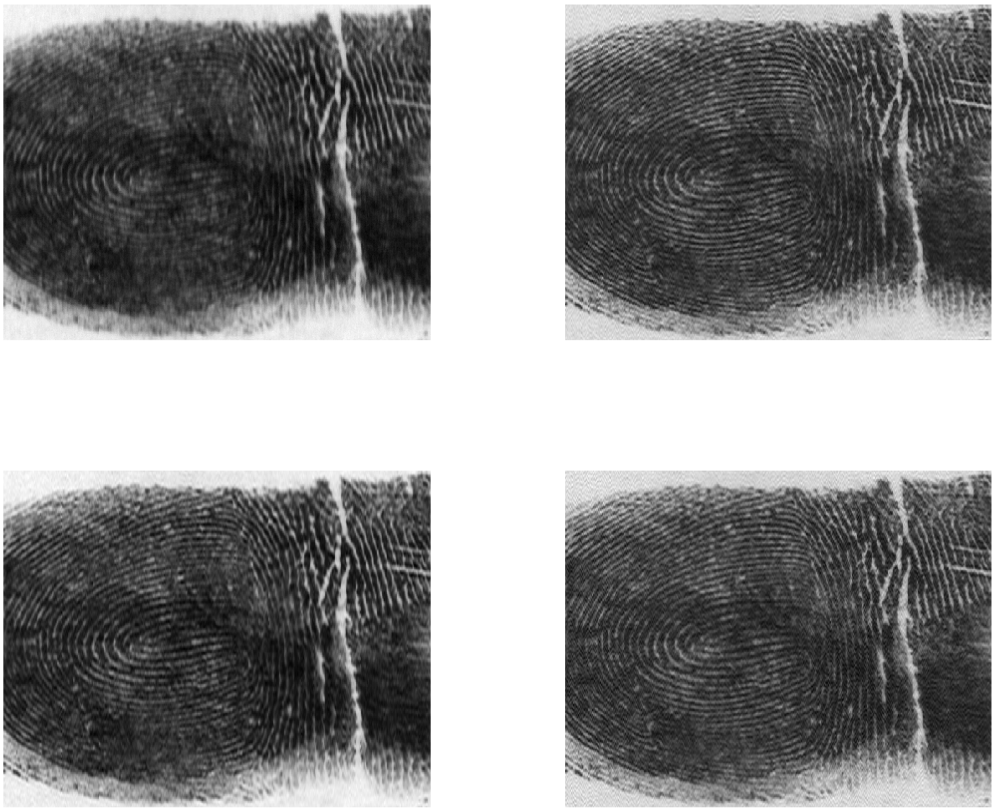

Figure 17: **Fmbmn** example. Top left: blurred noised image. Top right: image restored by MP. Bottom left: image restored by TRA. Top right: image restored by WA. The spline wavelet packets of fourth order from scales 2 to 6 were used.

The PSNR values are given in Table 3.

Input image	MP rest.	TRA rest.	WA rest.
26.3080	**29.1481**	28.1793	28.5150

Table 3: **Fmbmn** example. PSNR values

Figures 18 and 19 display restoration of column 200 and column 110, respectively by different deconvolution methods.

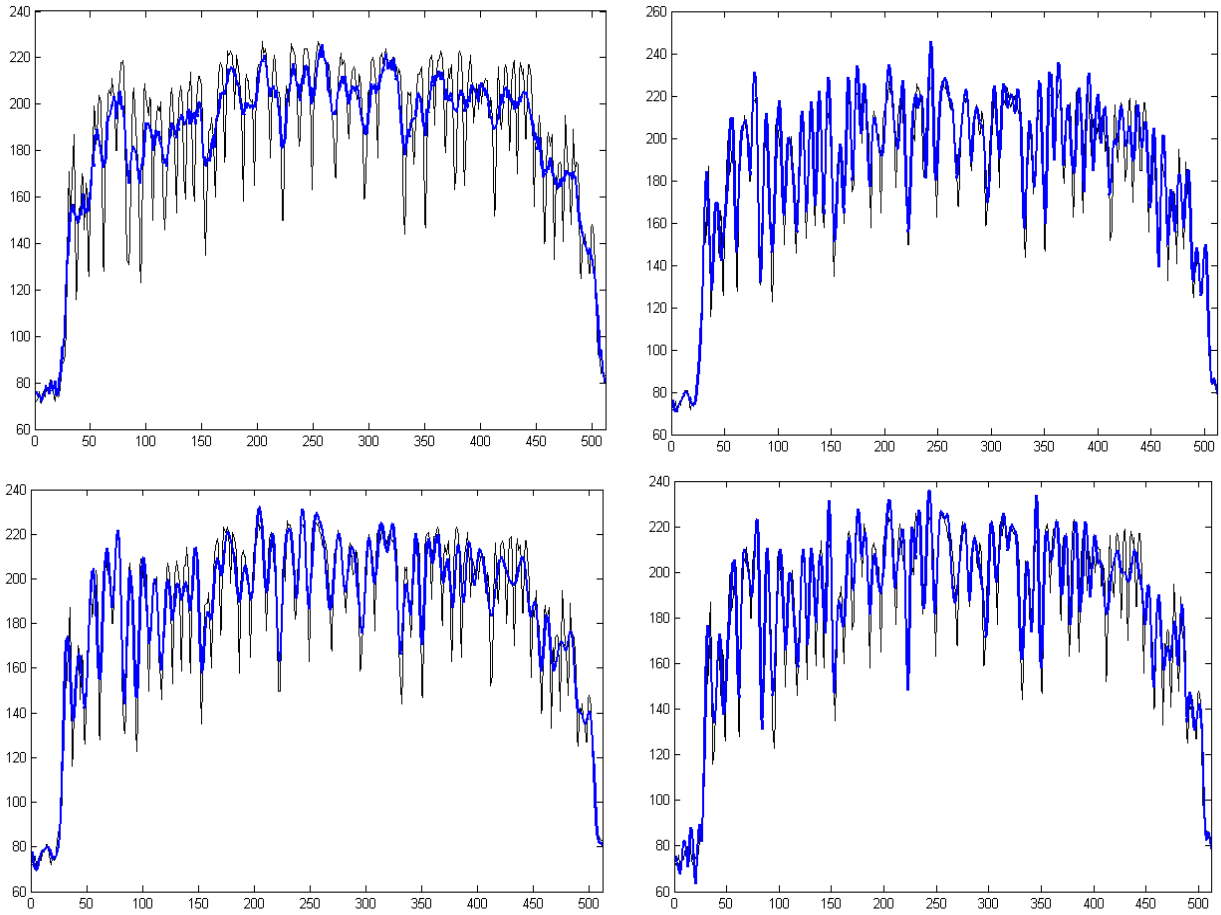

Figure 18: **Fmbmn** example. Top left: blurred noised column 200. Top right: column 200 restored by MP. Bottom left: column 200 restored by TRA. Top right: column 200 restored by WA. The thin line in all the figures depicts the original signal.

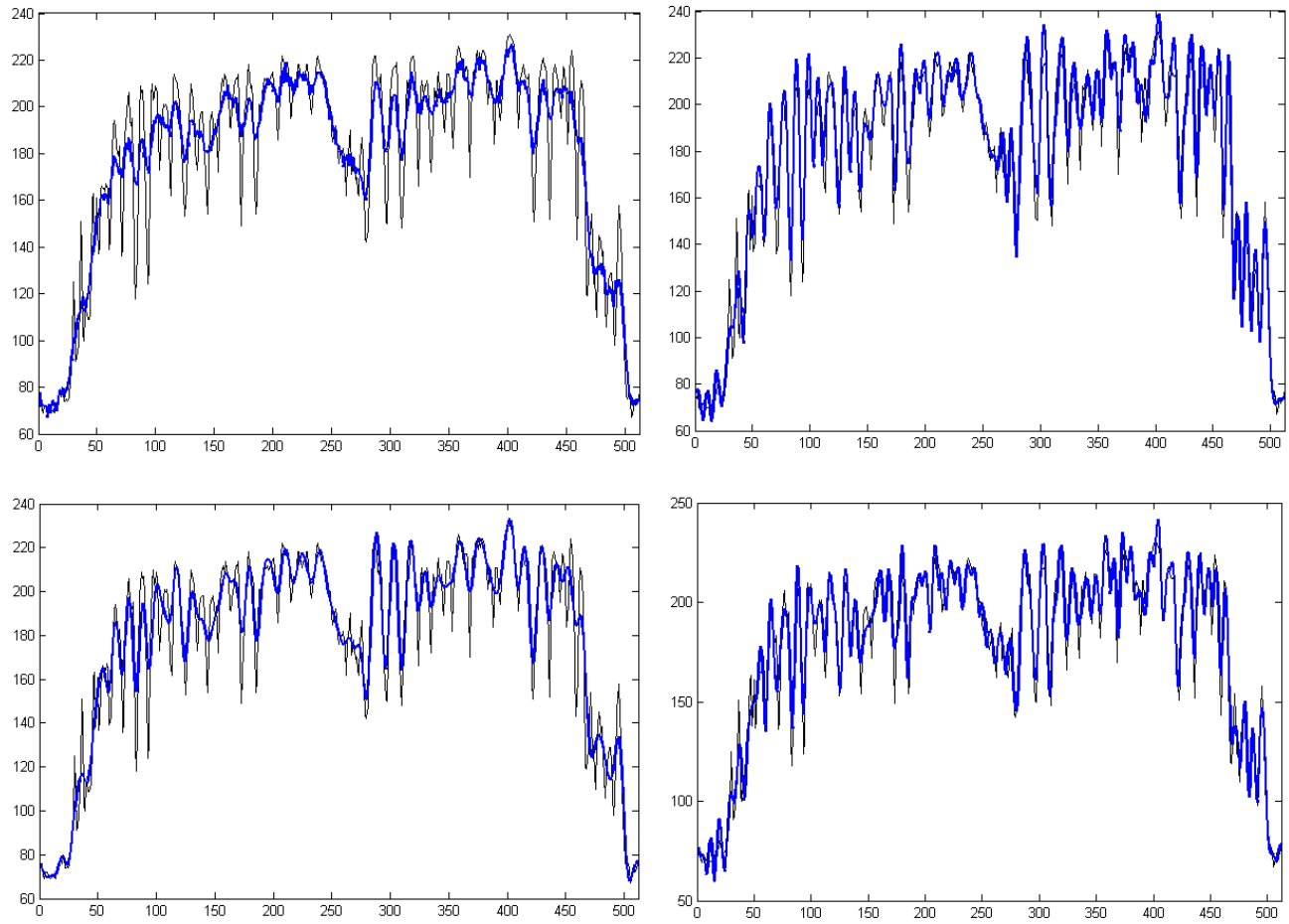

Figure 19: **Fmbmn** example. Top left: blurred noised column 110. Top right: column 110 restored by MP. Bottom left: column 110 restored by TRA. Top right: column 110 restored by WA. The thin line in all the figures depicts the original signal.

Observations:

1. The highest PSNR is produced by the MP restoration of columns. It exceeds the WA PSNR by 0.63 dB but, visually, the MP and WA restored images are hardly distinguishable.
2. Practically all details are restored in spite of strong blurring of the input image.
3. Comparing restoration of column 200 and of column 110 by different algorithms, we observe that MP provides restoration of the curves very close to the original while WA misses some events and, the more so, TRA.

Btsbmn example - Boats with strong blurring and moderate noise: In this experiment, the columns of the Boats image (Fig. **??**) were blurred using Gaussian kernel whose STD

was $\sigma_k = 5$ and corrupted by Gaussian white noise whose STD was $\sigma_n = 5$.

Figure 20: **Btsbmn** example: Boats.

Figure 21 displays the image whose columns are blurred and corrupted by noise and its restoration by different deconvolutionmethods.

Figure 21: **Btsbmn** example. Top left: blurred noised image. Top right: image restored by MP. Bottom left: image restored by TRA. Top right: image restored by WA. The spline wavelet packets of fourth order from scales 2 to 6 were used.

The PSNR values are given in Table 4.

Input image	MP rest.	TRA rest.	WA rest.
24.5668	**26.9429**	26.1924	26.8891

Table 4: **Btsbmn** example. PSNR values

Figures 22 and 23 display restoration of column 200 and column 110, respectively by different deconvolution methods.

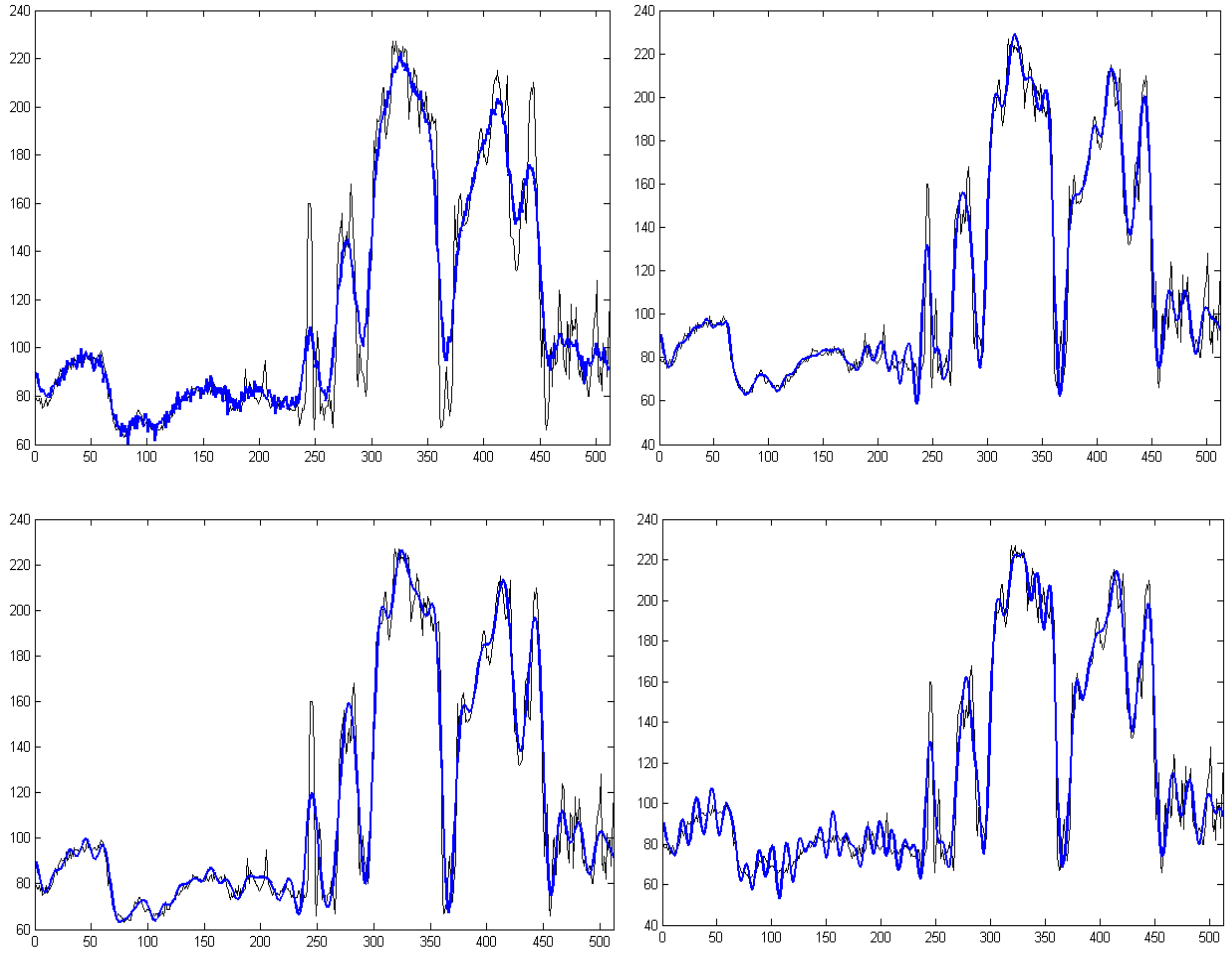

Figure 22: **Btsbmn** example. Top left: blurred noised column 160. Top right: column 160 restored by MP. Bottom left: column 160 restored by TRA. Top right: column 160 restored by WA. The thin line in all the figures depicts the original signal.

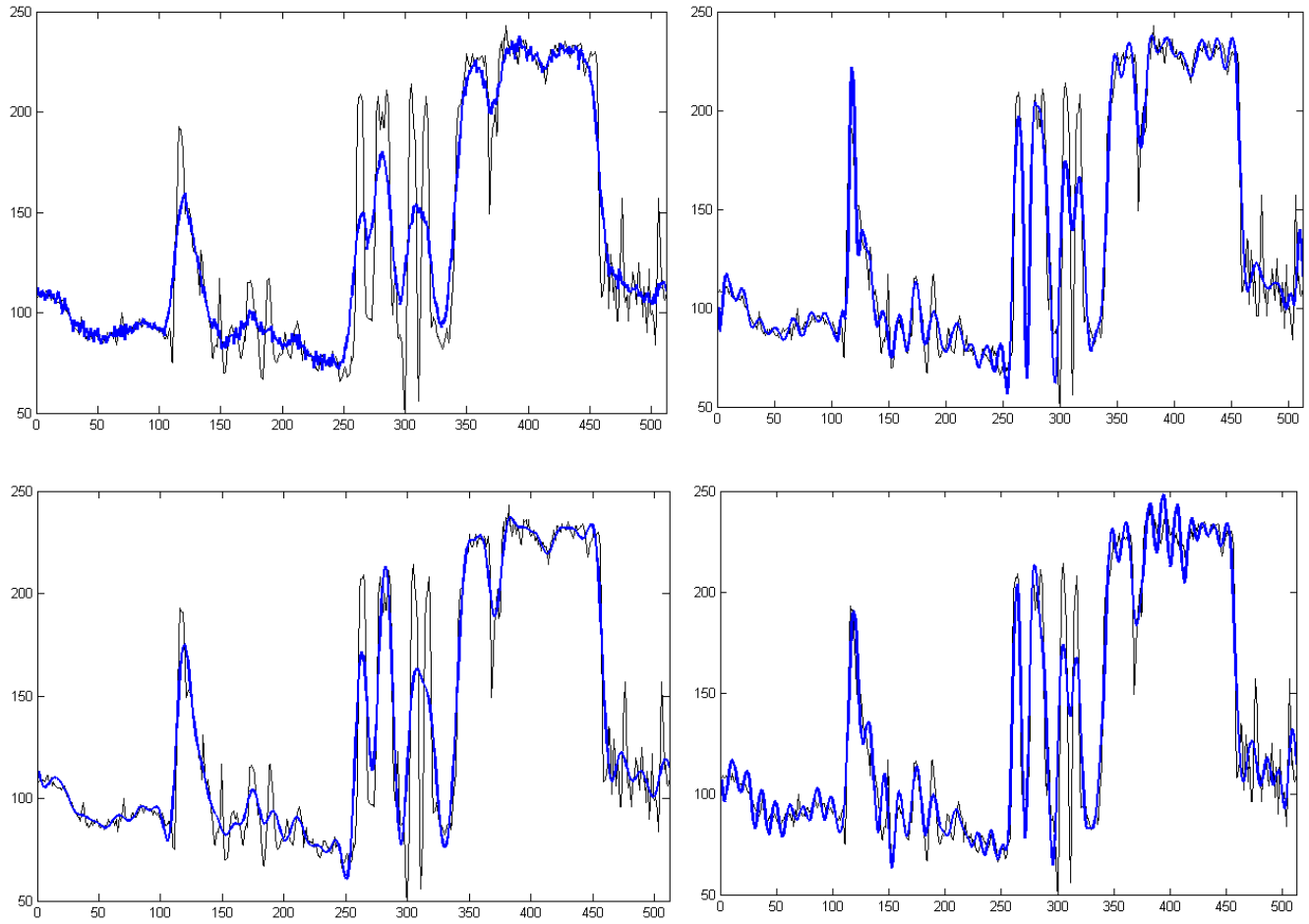

Figure 23: **Btsbmn** example. Top left: blurred noised column 364. Top right: column 364 restored by MP. Bottom left: column 364 restored by TRA. Top right: column 364 restored by WA. The thin line in all the figures depicts the original signal.

Observations:

1. The highest PSNR is produced by the MP restoration of columns. Although it exceeds the WA PSNR by only 0.05 dB but, visually, the MP restored image looks smoother compared to WA.
2. Practically all details are restored in spite of strong blurring of the input image.
3. Comparing restoration of column 160 and of column 364 by different algorithms, we observe that, unlike TRA, which is oversmoothed, MP and WA resolve most of the curves events. However the WA restored curves contain oscillating artifacts, which is not the case for MP.

6 Conclusions

This paper presents an efficient algorithm to restore signals from strongly noised blurred discrete data. The computational engine, which enables the construction of versatile libraries of spline wavelet packets dictionaries for matching pursuit (MP) and efficient implementation of the algorithm, is the Spline Harmonic Analysis (SHA). SHA imposes an harmonic analysis methodology onto the spline spaces. The operations of convolution and finding the projection coefficients become straightforward. The usage of splines enables to map the discrete noised data into the spaces of continuous functions, which approximate the sought after solution in the necessary smoothed class. The main distinctions from the conventional MP are:

1. Different dictionaries are used for testing the data and to approximate the solution.

2. Oblique projection of the data onto the dictionary elements instead of the conventional orthogonal projections are used. This produces a regularizing effect. An efficient automatic stopping rule is devised.

The conducted experiments confirmed efficiency of the algorithm. The algorithm was able to extract the coherent structure of signals, which were subjected to the presence of the strong blurring and immersed into deep noise. It provides sparse representations of solutions. Comparison with the conventional Tikhonov and Wiener deconvolution algorithm demonstrated the advantages of the presented algorithm.

However, direct extension of the algorithm to image processing appears computationally expensive. A somewhat related fast algorithm for image processing, which is based on 2D spline wavelet packets, was developed in [6]. In addition, we plan to combine the MP with the dissipation edge enhancement method [4] and time stepping image enhancement [5].

Glossary

1. $B^p(x)$ –the centered $N-$periodic B-spline of order p on the grid $\{k\}$.

2. ${}^p\mathcal{S}$ – the space of $N-$periodic splines of order p on the grid $\{k\}$.

3. $\beta_n^p(x)$ – the *exponential splines* of order p on the grid $\{k\}$, (2.7).

4. $\gamma_n^p(x)$ – the normalized *exponential splines* of order p on the grid $\{k\}$. (2.15).

5. $u_n^p \triangleq \beta_n^p(0) = \sum_{k=0}^{N-1} \omega^{-nk}\, B^p(k)$, (2.10).

6. $U_n^{p,q} \triangleq \sqrt{u_n^{2(p+q)} / \, u_n^{2p}\, u_n^{2q}}$, (2.17).

7. $V_n^p \triangleq u_n^p / \sqrt{u_n^{2p}}$, (2.18).

8. $Q_n^{p,q} \triangleq U_n^{p,q}\, V_n^{p+q} = u_n^{p+q} / \sqrt{u_n^{2p}\, u_n^{2q}}$, (2.24).

9. ${}^p\beta_n^{r,0}(x)$ – the *exponential splines* of order p on the grid $\{2^r k\}$, (3.2).

10. ${}^p u_n^r \triangleq {}^p\beta_n^{r,0}(0)$, (3.5).

11. ${}^p\gamma_n^{r,0}(x)$ – the normalized *exponential splines* of order p on the grid $\{2^r k\}$, (3.6).

12. $b_n^{r-1,0}$ and $b_n^{r-1,1}$ – filters for two-scale equations, (3.8) and (3.10).

13. ${}^p\mathcal{S}^{r,l}$ – orthogonal subspaces of space ${}^p\mathcal{S}$ (Section 3.1.3).

14. ${}^p\gamma^{r,l}(x) \in {}^p\mathcal{S}^{r,l}$ – orthonormal basis splines.

15. $\psi^{r,l}(x) \in {}^p\mathcal{S}^{r,l}$ –wavelet packets (3.17).

References

[1] J. H. Ahlberg, E. N. Nilson and J. L. Walsh, The theory of splines and their applications, New York, Acad. Press, 1967.

[2] A. Averbuch, V. Zheludev *Construction of biorthogonal discrete wavelet transforms using interpolatory splines*, Applied and Comp. Harmonic Analysis, **12**, (2002), 25-56.

[3] A. Averbuch and V. Zheludev, *Spline-based deconvolution,* Signal Processing, **89**, 1782-1797 (2009).

[4] A. Averbuch, B. Epstein, N. Fishelov, E. Turkel, *Edge enhancement postprocessing using artifical dissipation*, IEEE Trans. on Image Proc., **15(6)**, (2006), 1486-1498.

[5] A. Averbuch, R. Coifman, D. Donoho, M. Israeli, Y. Tsaig, *Image enhancement via time stepping*, available at http://www.cs.tau.ac.il/ amir1.

[6] A. Averbuch, V. Zheludev, P. Neittaanmäki and J. Koren, *Block based deconvolution algorithm using spline wavelet packets* to appear in Journal of Mathematical Imaging and Vision.

[7] G. Battle, A block spin construction of ondelettes.Part I. Lemarié functions, *Comm. Math. Phys.* **110** (1987), 601-615.

[8] M. Bertero and P. Boccacci. *Introduction to inverse problems in imaging.* 1998.

[9] C. De Mol and M. Defrise, *A note on wavelet-based inversion methods.* Inverse problems, image analysis and medical imaging, 2002.

[10] I. Daubechies, M. Defrise and C. De Mol. *An iterative thresholding algorithm for linear inverse problems with a sparsity constraint.* Communications on pure and applied mathematics, 2004

[11] M.A.T. Figueiredo and R.D. Nowak. *An EM algorithm for wavelet-based image restoration.* IEEE Trans. image processing, 2003.

[12] C. Charles, G. Leclerc, P. Louette, J.-P. Rasson and J.-J. Pireaux, *Noise filtering and deconvolution of XPS data by wavelets and Fourier transform,* Surface and Interface Analysis, **36**, (2004), 71-80.

[13] G.M. Davis, S. Mallat and M. Avelanedo, *Greedy adaptive approximation*, J. of Constr. Approx., **13**, (1997), 57–98.

[14] D. L. Donoho, *Nonlinear solution of linear inverse problems by wavelet-vaguelette decomposition,* Appl. Comp. Harm. Anal., **2**, (1995), 101–126.

[15] J. Fan, J.-Y. Koo, *Wavelet deconvolution,* IEEE Trans. Inf. Th., **48(3)**, (2002), 734–747.

[16] Janssen, A. J. E. M. *The Zak Transform: A Signal Transform for Sampled Time-Continuous Signals,* Philips J. Res. **43**, (1988), 23-69.

[17] R. Lattês and J.-L. Lions, *Méthode de quasi-réversibilité et applications,* Dunod, Paris, 1967.

[18] Lemarié, P. G., *Ondelettes à localization exponentielle,* J. de Math. Pure et Appl. **67** (1988) 227-236.

[19] S. Mallat and Z. Zhang, *Matching pursuit with time-frequency dictionaries,* IEEE Trans. Sign. Proc., **41**(12) (1993), 3397-3415.

[20] S. Mallat *A wavelet tour on signal processing,* Acad. Press, 1999.

[21] R, Neelamani, H. Choi and R. Baraniuk, *ForWaRD: Fourier-wavelet regularized deconvolution for ill-conditioned systems*, IEEE Trans. Sign. Proc., **52(2)**, (2004), 418–433.

[22] D. L. Philips, *A technique for the numerical solution of certain integral equations of the first kind,* J. Assoc. Comp. Mach. **9(1)**, (1962), 84-97.

[23] Y. C. Pati R. Rezaiifar, P. S. Krishnaprasad, *Orthogonal matching pursuit: recursive function approximation with applications to wavelet decomposition*, in Proceedings of the 27 th Annual Asilomar Conference on Signals, Systems, and Computers, (1993)

[24] G. Plonka, M. Tasche, *On the computation of periodic spline wavelets.* Applied and Computational Harmonic Analysis 2 (1995), 1-14.

[25] I. J. Schoenberg , Cardinal spline interpolation, CBMS, **12**, SIAM, Philadelphia, 1973.

[26] H. Takeda, S. Farsiu, and P. Milanfar, *Deblurring Using Regularized Locally Adaptive Kernel Regression*, IEEE Trans. Image Proc., **17(4)**, (2008), 550–563.

[27] A. N. Tikhonov, *Solution of incorrectly formulated problems and the regularization method,* Soviet Math. Dokl., **4**, (1963), 1035.

[28] A. N. Tikhonov and V. Y. Arsenin, *Solution of ill-posed problems,* New York: Wiley, 1977.

[29] C. Vonesch and M. Unser, *A Fast Thresholded Landweber Algorithm for Wavelet-Regularized Multidimensional Deconvolution*, IEEE Trans. Image Proc., **17(4)**, (2008), 539–549.

[30] J. G. McNally, T. Karpova, J. Cooper, and J. A. Conchello, *Three-dimensional imaging by deconvolution microscopy*, Methods, **19(3)**, (1999), 373385.

[31] C. Vonesch, F. Aguet, J.-L. Vonesch, and M. Unser, *The colored revolution of bioimaging,* IEEE Signal Process. Mag., **23(3)**, (2006) 2031.

[32] C. Vogel, *Computational methods for inverse problems*, SIAM, 2002.

[33] N. Wiener, Extrapolation, interpolation and smoothing of stationary time series with engineering applications, Wiley, New York, 1949.

[34] J. Zak, *Finite translations in solid-state physics,* Phys. Rev. Lett., **19**, no. 4, (1967), 1385-1387.

[35] V. A. Zheludev, *An operational calculus connected with periodic splines,* Soviet. Math. Dokl. **42** (1991), 162-167.

[36] V. A. Zheludev, *Periodic splines and the fast Fourier transform,* Comput. Math. & Math Phys. **32**, (1991), 149-165.

[37] V. A. Zheludev *Spline-operational calculus and numerical solving convolution integral equations of the first kind*, Differ. Equations **28** (1992), 269-280.

[38] V. A. Zheludev, *Spline-operational calculus and inverse problem for heat equation,* Proc. Int. Conf. *Approximation Theory*, Kecskemét, Hungary, 1990, (J. Szabados, K. Tandoi eds.,) Colloq. Math. Soc. J.Bolyai, **58**, (1991), 763-783.

[39] V. A. Zheludev, *Periodic splines, harmonic analysis, and wavelets.* in "Signal and image representation in combined spaces, 477–509, Wavelet Anal. Appl., 7," (eds. Y. Y. Zeevi and R. Coifman), Academic Press, San Diego, CA, 1998.

[40] V. A. Zheludev, *Integral representation of slowly growing equidistant splines*, Approximation Theory and Applications, **14**, no. 4, (1998), 66-88.

[41] V. A. Zheludev, *Wavelet analysis in spaces of slowly growing splines via integral representation*, Real Analysis Exchange, **24**, (1998/99), 229-261.

[42] V. A. Zheludev, *Interpolatory subdivision schemes with infinite masks originated from splines,* Advances in Comp. Math. **25**,(2006), 475–506.

[43] V. A. Zheludev, A. Z. Averbuch, *Computation of interpolatory splines via triadic subdivision,* Advances in Comp. Math. Volume 32, Issue 1 (2010), 63-72.